Tunable range of terahertz oscillations triggered by the spin Hall effect in a biaxial antiferromagnet

Ya-Qi Zhao, Peng-Bin He, * and Meng-Qiu Cai
School of Physics and Electronics, Hunan University, Changsha 410082, China

(Received 28 June 2022; revised 10 October 2022; accepted 12 October 2022; published 24 October 2022)

We present a theoretical study on the current and frequency windows of self-oscillations induced by the dampinglike spin-orbit torque in a biaxial antiferromagnet. By the linear stability analysis and averaging technique, we analytically formulate the lower and upper thresholds and the frequency of self-oscillations. We find that the self-oscillation range is highly sensitive to the damping and magnetic anisotropies, which have a variety of options in abundant antiferromagnets. Beyond a critical damping, the self-oscillation can arise after the instability of an antiferromagnetic state, with its range widening for a heavier damping. Below it, a spin-flip transition occurs when increasing the current, similar to the spin flip under an increasing magnetic field. Meanwhile, we examine the role of anisotropies. With the spin polarization along the easy axis, the weak easy- and hard-axis anisotropies allow self-oscillations, the range of which is broadened for weaker anisotropies. At the same time, the spin-flip transition is permitted for strong anisotropies. If the spin polarization coincides with the hard axis, the transition types are mainly determined by the easy-axis anisotropy. For a weak easy-axis anisotropy, the self-oscillation can develop with its range expanding for a stronger hard-axis anisotropy. Finally, we envision that (tunneling) anisotropic magnetoresistance may act as an effective means to probe the oscillations.

DOI: 10.1103/PhysRevB.106.134427

I. INTRODUCTION

Self-oscillation is a ubiquitous nonlinear phenomenon [1], where a periodic motion is self-sustained under a nonperiodic driving force. For a magnetic system, this driving force can be spin torques, including spin-transfer torques [2] and spin-orbit torques (SOTs) [3]. This magnetic self-oscillation produces sustainable ac signals from dc inputs, acting as spin-torque oscillators. For the past two decades, with the aim of developing microwave emitters [4,5], intensive research efforts [6–17] have been deployed to understand the properties of ferromagnetic self-oscillations, such as the phase diagram [6–8], the thermal effects [6,12], the threshold currents [9,10,15,16], the stability [11,13,14,16], and the relaxation [17]. In a single-domain ferromagnet (FM), when the dampinglike spin torque balances the damping on average, the magnetization precession is propelled by the anisotropy fields or the external magnetic fields, with frequencies of the order of a few gigahertz.

Terahertz (THz) waves, because their frequency range has not been technologically exploited and has fascinating potentials for many applications, are attracting increasing attention from the spintronics community. Obviously, it is impractical to generate THz oscillation in FMs. So, the focus in recent years has been shifting towards the films and multilayers with antiferromagnetic (AFM) coupling. Considerable efforts have been made on the self-oscillation or linear oscillation in synthetic [18–22], collinear [23–37], and noncollinear AFMs [38–42], as well as ferrimagnets [43–45]. In these devices, when the adjacent magnetic moments are inclined relative to one another, the strong exchange torques drive their precession. Furthermore, when the damping is compensated for by the dampinglike spin torque, a self-oscillation arises, the frequency of which is in the THz region in view of the strong exchange.

In particular, some interesting results have been achieved for collinear AFMs. For example, in the strong exchange limit, the oscillation frequency is proportional to the spin-torque strength, while it is inversely proportional to the damping constant [23,25,27,33,37]. It can be concluded that the exchange interaction mainly propels the precession in the promise of an average balance between the spin torque and the damping. The oscillations can be adjusted by the spin-polarization directions [33] and a weak Dzyaloshinskii-Moriya interaction [27,30,31]. The lower and upper thresholds of self-oscillation have been derived analytically for uniaxial AFM [37]. In addition, given the abundance of AFM materials, these works investigate AFMs with different types of magnetic anisotropy, including the uniaxial [30,31,33,36,37] and biaxial [23–25,27,34] AFMs, the AFM with a perpendicular uniaxial anisotropy and an in-plane fourfold symmetric anisotropy [32], as well as the AFM with biaxial and cubic anisotropies [35].

While extensive work has already been performed on the self-oscillation of collinear AFMs, the influences of damping and anisotropies on the range of self-oscillation remain poorly understood. Considering the diversity of AFM materials [46], different anisotropies and damping can be chosen, which can be used to adjust the current to excite a self-oscillation and its frequency. These properties are essential for successful application of spin-torque nano-oscillators in THz signal generation. Therefore, in this paper, for two cases with spin polarization along the easy or the hard axis, the thresholds

*hepengbin@hnu.edu.cn

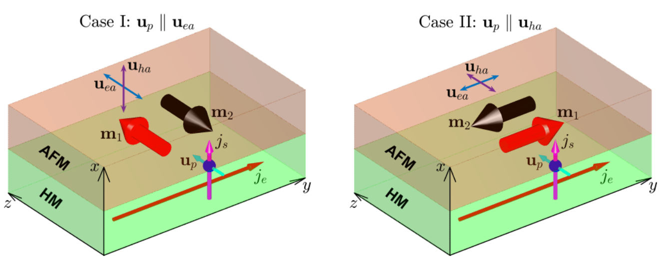

FIG. 1. Sketch of HM/AFM bilayer with the spin polarization ($\mathbf{u}_p$) along the easy axis ($\mathbf{u}_{\text{ea}}$) or the hard axis ($\mathbf{u}_{\text{ha}}$). j_e and j_s are the electric and spin currents.

are calculated analytically by the linear stability analysis and averaging technique (Melnikov's method) [47,48]. The latter is fit for analyzing the self-oscillation of a weakly perturbed system with periodic orbits. For the ferromagnetic self-oscillations, the good agreement between the analytical and numerical results substantiates the validity of this averaging technique [7–17]. Moreover, apart from the thresholds, the frequencies are also derived by the averaging technique. Based on these analytical expressions, we will investigate the effects of damping and anisotropies on the current and frequency windows of self-oscillations.

The paper is organized as follows. After the introduction Sec. I and a model description Sec. II, we formulate the thresholds and frequency of self-oscillations for the case with the spin polarization along the easy axis, and we analyze its current and frequency ranges; see Sec. III supplemented with Appendixes A and C. Then, similar derivations and analyses are performed for the case with the spin polarization along the hard axis; see Sec. IV supplemented with Appendixes B, D, and E. In Sec. V, we calculate the self-oscillation thresholds and the corresponding frequencies for several typical AFMs, and we discuss the possible detecting approaches. Section VI is devoted to conclusions.

II. MODEL

We consider a bilayer consisting of a heavy metal (HM) layer acting as a spin-current source and a layer of an AFM with biaxial anisotropy; see Fig. 1. According to the mechanism of the spin Hall effect [3], when the electric current flows through the HM layer, the spin-orbit interaction causes a deflection of electrons according to their spin orientations into opposite directions. This transverse spin current exerts a spin-orbit torque (SOT) on the AFM layer. Magnetization dynamics in this AFM layer is ruled by a pair of Landau-Lifshitz-Gilbert-Slonczewski (LLGS) equations,

$$\frac{d\mathbf{m}_i}{dt} = \mathbf{m}_i \times \frac{d\mathcal{E}}{d\mathbf{m}_i} + \alpha \mathbf{m}_i \times \frac{d\mathbf{m}_i}{dt} + \boldsymbol{\tau}_i, \tag{1}$$

where two unit vectors $\mathbf{m}_i$ $(i = 1, 2)$ represent the directions of the sublattice magnetic moments, and α is the Gilbert damping constant.

The magnetic energy includes the contributions from the antiparallel exchange coupling and the biaxial anisotropy,

$$\mathcal{E} = \omega_{\text{ex}} \mathbf{m}_1 \cdot \mathbf{m}_2 - \omega_{\text{ea}} \sum_i (\mathbf{m}_i \cdot \mathbf{u}_{\text{ea}})^2 + \omega_{\text{ha}} \sum_i (\mathbf{m}_i \cdot \mathbf{u}_{\text{ha}})^2, \tag{2}$$

where the exchange, easy-, and hard-axis anisotropic energies are scaled in units of the frequency. Expressed by corresponding effective fields, they are $\omega_{\text{ex}} = \gamma H_{\text{ex}}$, $\omega_{\text{ea}} = \gamma H_{\text{ea}}$, and $\omega_{\text{ha}} = \gamma H_{\text{ha}}$, with γ being the magnitude of the gyromagnetic ratio. The unit vectors $\mathbf{u}_{\text{ea}}$ and $\mathbf{u}_{\text{ha}}$ denote the directions of easy and hard axes. Here, the shape anisotropy (demagnetization effect) is not considered, because the normal component of the total magnetization ($\mathbf{m} = \mathbf{m}_1 + \mathbf{m}_2$) is zero, as derived in the following sections.

The dampinglike SOT is written as

$$\boldsymbol{\tau}_i = -\omega_{\text{SOT}} \mathbf{m}_i \times (\mathbf{m}_i \times \mathbf{u}_p). \tag{3}$$

Here, the strength of SOT is also scaled by the frequency, which is

$$\omega_{\text{SOT}} = \frac{\mu_B}{eM_s d} \xi j_e, \tag{4}$$

with d being the thickness of the AFM layer, μ_B the Bohr magneton, e the element charge, M_s the sublattice saturation magnetization, and j_e the electric current density. ξ is the SOT efficiency, which is equal to $T_{\text{int}}\theta_{\text{sh}}$ [49,50], with θ_{sh} being the spin Hall angle, and T_{int} the spin transparency of the interface [51]. $\mathbf{u}_p$ is the unit vector of the spin polarization, which is perpendicular to both directions of the spin current and the charge current.

III. CASE I: $\mathbf{u}_p \parallel \mathbf{u}_{\text{ea}}$

For this case, we choose a coordinate system in which the easy axis ($\mathbf{u}_{\text{ea}}$) and the spin polarization ($\mathbf{u}_p$) are along the z direction, and the hard axis ($\mathbf{u}_{\text{ha}}$) is along the x direction, as shown in Fig. 1.

A. Lower and upper thresholds of the self-oscillation

Now, we define the stability regions of all the stable equilibria, which can be confirmed from numerical integration of the coupled LLGS equations [Eq. (1)] for case I. As detailedly derived in Appendix A, solving the equilibrium equation defined by $d\mathbf{m}_i/dt = 0$ yields two kinds of stable equilibria.

One is two equivalent AFM states with $\mathbf{m}_1$ along the z ($-z$) direction and $\mathbf{m}_2$ along the $-z$ (z) direction. Utilizing the linear stability analysis (see Appendix A 1 for detailed derivations), this equilibrium is stable if $|\omega_{\text{SOT}}| < \omega_{\text{SOT}}^l$, where

$$\omega_{\text{SOT}}^l = \frac{1}{\sqrt{2}} \sqrt{\sqrt{4\omega_{\text{ha}}^2 \omega_{\text{ex}}^2 + A_+^2} - A_-}, \tag{5}$$

with

$$\begin{aligned} A_\pm = {} & (\omega_{\text{ex}} + 2\omega_{\text{ea}})(\omega_{\text{ex}} + 2\omega_{\text{ea}} + 2\omega_{\text{ha}}) \\ & \pm \alpha^2 (2\omega_{\text{ea}} + \omega_{\text{ha}})(2\omega_{\text{ex}} + 2\omega_{\text{ea}} + \omega_{\text{ha}}). \end{aligned} \tag{6}$$

In the absence of the hard-axis anisotropy, Eq. (5) is reduced as $\omega_{\text{SOT}}^l = 2\alpha\sqrt{\omega_{\text{ea}}(\omega_{\text{ex}} + \omega_{\text{ea}})}$, which coincides with the result of the uniaxial AFM in Ref. [37].

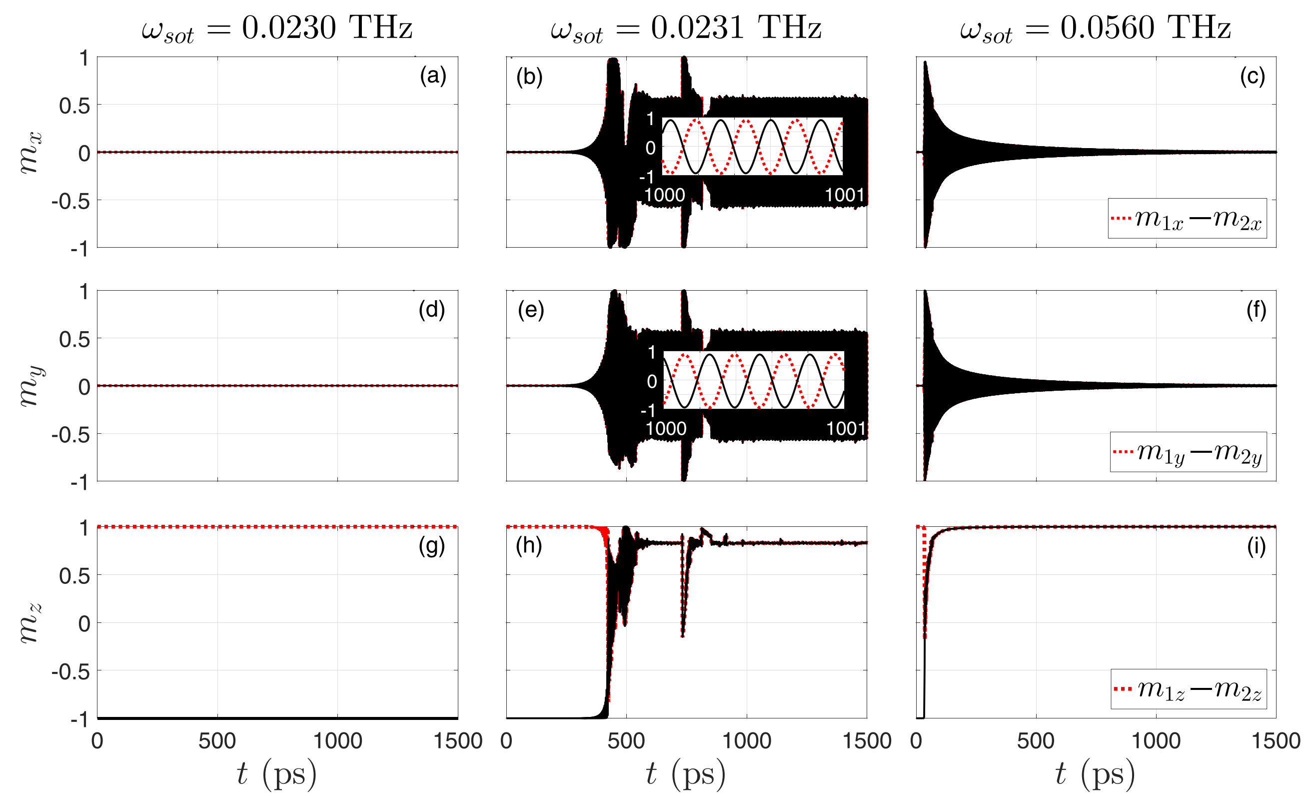

FIG. 2. Evolutions of x-components (upper panel), y-components (middle panel), and z-components (lower panel) of $\mathbf{m}_{1,2}$ for the AFM state (the first column), the precession (the second column), and the FM state (the third column) of case I. The parameters of NiO [52,53] are adopted: $\omega_{\rm ex} = 27.4$ THz, $\omega_{\rm ea} = 1$ GHz, $\omega_{\rm ha} = 23$ GHz, and $\alpha = 0.001$. Putting these parameters into Eqs. (5) and (7), the lower and upper thresholds of precession are $\omega^l_{\rm SOT} = 0.0230$ THz and $\omega^u_{\rm SOT} = 0.0548$ THz, which are in good agreement with the numeric results. The insets show the evolutions in the time interval between 1000 and 1001 ps. Here, $\mathbf{m}_1$ ($\mathbf{m}_2$) coincides with $\mathbf{u}_p$ ($-\mathbf{u}_p$) initially.

The others are two FM states with $\mathbf{m}_{1,2}$ along the z or $-z$ direction. Using the same method (see Appendix A 2 for detailed derivations), the stability condition of these equilibria is derived as $|\omega_{\rm SOT}| > \omega^u_{\rm SOT}$, where

$$\omega^u_{\rm SOT} = \alpha(2\omega_{\rm ex} - 2\omega_{\rm ea} - \omega_{\rm ha}). \tag{7}$$

In the above derivations, the exchange interaction is assumed to be much stronger than the easy- and hard-axis anisotropies.

The other two kinds of equilibria are unstable for all values of $\omega_{\rm SOT}$ (see Appendixes A 3 and A 4 for details) and are not considered in the main text.

If $\omega^l_{\rm SOT} < \omega^u_{\rm SOT}$, in the interval that $\omega^l_{\rm SOT} < |\omega_{\rm SOT}| < \omega^u_{\rm SOT}$, there is no stable equilibrium. So, in this region, a precessional state may emerge. This can be justified by integrating Eq. (1) numerically, as exemplified in Figs. 2(b), 2(e), and 2(h).

Below $\omega^l_{\rm SOT}$, the system remains in the stationary AFM state, as shown in Figs. 2(a), 2(d), and 2(g). Inevitably, $\mathbf{m}_1$ ($\mathbf{m}_2$) oscillates slightly around $\mathbf{e}_z$ ($-\mathbf{e}_z$), generating a linear mode.

Across the lower threshold, there is a discontinuous change of the magnetization direction, similar to the spin-flop transition [54,55] of AFMs under an applied magnetic field parallel to the sublattice magnetization. This transition comes from the instability of the linear mode [24], which breaks the static equilibrium among the SOT, the exchange torque, and the anisotropic ones. Then, for a positive (negative) $\omega_{\rm SOT}$, the SOT slants $\mathbf{m}_2$ ($\mathbf{m}_1$) to $\mathbf{e}_z$ ($-\mathbf{e}_z$). Correspondingly, the emerging exchange torque between $\mathbf{m}_1$ and $\mathbf{m}_2$ propels their precession around $\mathbf{e}_z$ or $-\mathbf{e}_z$, producing a self-oscillation.

If $\omega_{\rm SOT} > \omega^u_{\rm SOT}$ ($\omega_{\rm SOT} < -\omega^u_{\rm SOT}$), $\mathbf{m}_2$ ($\mathbf{m}_1$) flips to $\mathbf{e}_z$ ($-\mathbf{e}_z$), as shown by Figs. 2(c), 2(f), and 2(i).

B. Frequency of the self-oscillation

One interesting observation is that, during the self-oscillation, $\mathbf{m}_1$ and $\mathbf{m}_2$ remain antiphase. Namely, $m_{2x} = -m_{1x}$, $m_{2y} = -m_{1y}$, and $m_{2z} = m_{1z}$. This can be seen by comparing the insets of Figs. 2(b) and 2(e). On the other hand, when taking a substitution $m_{2x} \to -m_{1x}$, $m_{2y} \to -m_{1y}$, and $m_{2z} \to m_{1z}$, we find that the equation for sublattice 1 is equivalent to that for sublattice 2. Therefore, by setting

$$m_{1x} = -m_{2x} = n_x, \quad m_{1y} = -m_{2y} = n_y,$$
$$m_{1z} = m_{2z} = n_z, \tag{8}$$

we can transform the coupled LLGS equation [Eq. (1)] into a single-vector one, which makes it easy to analytically deal with the self-oscillations. Then, taking $\mathbf{u}_p = \mathbf{e}_z$, $\mathbf{u}_{\rm ea} = \mathbf{e}_z$, and $\mathbf{u}_{\rm ha} = \mathbf{e}_x$ (see Fig. 1), Eq. (1) is reduced as

$$\frac{d\mathbf{n}}{dt} = \mathbf{n} \times \frac{d\mathcal{E}_n}{d\mathbf{n}} + \alpha \mathbf{n} \times \frac{d\mathbf{n}}{dt} + \boldsymbol{\tau}_n. \tag{9}$$

Dropping an inessential constant, the reduced magnetic energy reads

$$\mathcal{E}_n = (\omega_{\rm ex} - \omega_{\rm ea})(\mathbf{n}\cdot\mathbf{e}_z)^2 + \omega_{\rm ha}(\mathbf{n}\cdot\mathbf{e}_x)^2. \tag{10}$$

In addition, the reduced SOT is

$$\boldsymbol{\tau}_n = -\omega_{\rm SOT}\mathbf{n}\times(\mathbf{n}\times\mathbf{e}_z). \tag{11}$$

To calculate the frequency of a self-oscillation, an averaging technique (referred to as Melnikov's method) [7–17,47,48] is applied to solve Eqs. (9)–(11). This method is suitable for treating the self-oscillation in weakly perturbed conservative systems. Here, in view of the strong AFM exchange, it is reasonable to assume the damping and the SOT as perturbations ($\omega_{\rm SOT}/\omega_{\rm ex} \lesssim 10^{-2}$ and $\alpha \lesssim 10^{-2}$ in our consideration). Then, when the energy supplied by the SOT balances with the dissipation due to the damping during a precession, a self-oscillation can be maintained. **n** approximately precesses along the orbits given by Eq. (10), which conserves the magnetic energy.

When **n** settles into a constant-energy orbit, an average balance between the energy gain and dissipation results in

$$\oint_\Gamma \frac{d\mathcal{E}_n}{dt}dt = -\mathcal{W}_{\rm damp} + \mathcal{W}_{\rm SOT} = 0, \tag{12}$$

where Γ denotes the precessional orbit. Omitting the high-order terms of α and $\omega_{\rm SOT}$, the energy dissipation $\mathcal{W}_{\rm damp}$ and supply $\mathcal{W}_{\rm SOT}$ read

$$\mathcal{W}_{\rm damp} = \alpha\oint_\Gamma\left(\mathbf{n}\times\frac{d\mathcal{E}_n}{d\mathbf{n}}\right)^2 dt, \tag{13}$$

$$\mathcal{W}_{\rm SOT} = \omega_{\rm SOT}\oint_\Gamma(\mathbf{n}\times\mathbf{e}_z)\cdot\left(\mathbf{n}\times\frac{d\mathcal{E}_n}{d\mathbf{n}}\right)dt. \tag{14}$$

Completing these two loop integrals (see Appendix C), the balance equation (12) gives the SOT strength $\omega_{\rm SOT}$ to excite a self-oscillation on the $\mathcal{E}_n$ orbit,

$$\omega_{\rm SOT}(\mathcal{E}_n) = \frac{4\alpha\sqrt{\mathcal{E}_n(\omega_{\rm ex}-\omega_{\rm ea})}}{\pi(\omega_{\rm ex}-\omega_{\rm ea}-\mathcal{E}_n)}[(\omega_{\rm ex}-\omega_{\rm ea}-\omega_{\rm ha})\mathsf{E}(k) - (\mathcal{E}_n-\omega_{\rm ha})\mathsf{K}(k)], \tag{15}$$

where $\mathsf{E}(k)$ and $\mathsf{K}(k)$ are the complete elliptic integrals of the second and first kinds, with the modulus

$$k = \sqrt{\frac{\omega_{\rm ha}(\omega_{\rm ex}-\omega_{\rm ea}-\mathcal{E}_n)}{\mathcal{E}_n(\omega_{\rm ex}-\omega_{\rm ea}-\omega_{\rm ha})}}. \tag{16}$$

When $\mathcal{E}_n$ approaches its maximum $\omega_{\rm ex}-\omega_{\rm ea}$, the limit of $\omega_{\rm SOT}$ [Eq. (15)] coincides with the threshold $\omega^u_{\rm SOT}$ [Eq. (7)].

Due to the balance between the SOT and the damping, the self-oscillation is driven by the exchange torque and the anisotropy ones. So, the precession period can be derived from the conservative parts of Eq. (9). As calculated in Appendix C, the frequency is

$$f(\mathcal{E}_n) = \frac{\sqrt{\mathcal{E}_n}\sqrt{\omega_{\rm ex}-\omega_{\rm ea}-\omega_{\rm ha}}}{2\mathsf{K}(k)}. \tag{17}$$

At the upper threshold, $\mathcal{E}_n = \omega_{\rm ex}-\omega_{\rm ea}$, and the corresponding frequency

$$f^u = \frac{1}{\pi}\sqrt{(\omega_{\rm ex}-\omega_{\rm ea})(\omega_{\rm ex}-\omega_{\rm ea}-\omega_{\rm ha})}. \tag{18}$$

Equations (15) and (17) give the dependence of f on $\omega_{\rm SOT}$ by eliminating $\mathcal{E}_n$. Due to the elliptic integrals in Eqs. (15) and (17), an explicit analytic relation between f and $\omega_{\rm SOT}$ is untractable for a general case. In the absence of the hard-axis anisotropy, $f = \omega_{\rm SOT}/(2\pi\alpha)$, which coincides with the result of Ref. [37].

C. Range of the self-oscillation

Here, based on Eqs. (5) and (7), we will discuss the influences of the damping and anisotropies on the range of $\omega_{\rm SOT}$ in which a self-oscillation exists. The corresponding range of the frequency can be analyzed by Eqs. (15) and (17). In view of the abundance of AFM materials [46] and in order to analyze the general features, the parameters used in the following discussion do not correspond to a specific substance, but they are estimated moderately in an experimentally feasible range.

First, let us talk about the effect of the damping on the range of self-oscillations. In Figs. 3(a)–3(c), we plot the surfaces of $\omega^l_{\rm SOT}$ and $\omega^u_{\rm SOT}$ on top of the $\omega_{\rm ea}$-$\omega_{\rm ha}$ plane for different α. In the spaces in which $\omega^l_{\rm SOT} < \omega_{\rm SOT} < \omega^u_{\rm SOT}$, there exist self-oscillations. Otherwise, the stationary states, such as AFM or FM states, exist. Additionally, as plotted in Fig. 3(g), the isosurface in α-$\omega_{\rm ea}$-$\omega_{\rm ha}$ parametric space, derived from $\omega^l_{\rm SOT} = \omega^u_{\rm SOT}$, separates the regions where the self-oscillations are allowed (above the surface) and cannot exist (below the surface). For certain α, this boundary degenerates to a curve in $\omega_{\rm ea}$-$\omega_{\rm ha}$ plane, corresponding to the contours in Figs. 3(a)–3(c). Comparing Figs. 3(a), 3(b), and 3(c), it can be observed that the self-oscillation range expands for stronger damping, as also shown by contour curves of $\omega^l_{\rm SOT} = \omega^u_{\rm SOT}$. This can be attributed to the balance between the SOT and the damping, which is necessary for a stable self-oscillation. For fixed anisotropies, if strengthening the damping, a much stronger SOT is needed to offset it. So, the range of $\omega_{\rm SOT}$ for self-oscillations is enlarged.

To illustrate the effect of the damping more clearly, we also show in Fig. 4(a) the dependence of the lower and upper thresholds on α while keeping the anisotropies unchanged. For small α, when increasing $\omega_{\rm SOT}$, the AFM state becomes unstable at the lower threshold $\omega^l_{\rm SOT}$. Then, one sublattice magnetization reverses, like the spin-flip transition [54] of an AFM induced by a magnetic field in the presence of a strong anisotropy. Namely, the system switches directly from an AFM state to a FM one. For a relatively large α, with $\omega_{\rm SOT}$ increasing, the two sublattice magnetizations ($\mathbf{m}_1$ and $\mathbf{m}_2$) start to precess at $\omega^l_{\rm SOT}$, as shown in Figs. 2(b), 2(e), and 2(h). There is a jump from the AFM state to a precession, where $\mathbf{m}_1$ and $\mathbf{m}_2$ form a cone around the spin polarization $\mathbf{u}_p$. This jump is similar to the spin-flop transition [54,55] of AFM induced by a magnetic field in the presence of a weak anisotropy. The difference is that the magnetic field-induced spin-flop state is static and nonprecessional. Because no external torques can offset the damping one, the precession cannot sustain. So, after reaching a balance between the exchange torque and the magnetic-field one, a static spin-flop state is arrived. Under the SOT, if increasing $\omega_{\rm SOT}$ further, the cone angle of precession decreases. Finally, the system enters the FM state at the upper threshold $\omega^u_{\rm SOT}$, as shown in Figs. 2(c), 2(f), and 2(i), just like the saturation of an AFM by further increasing the magnetic field beyond the spin-flop transition.

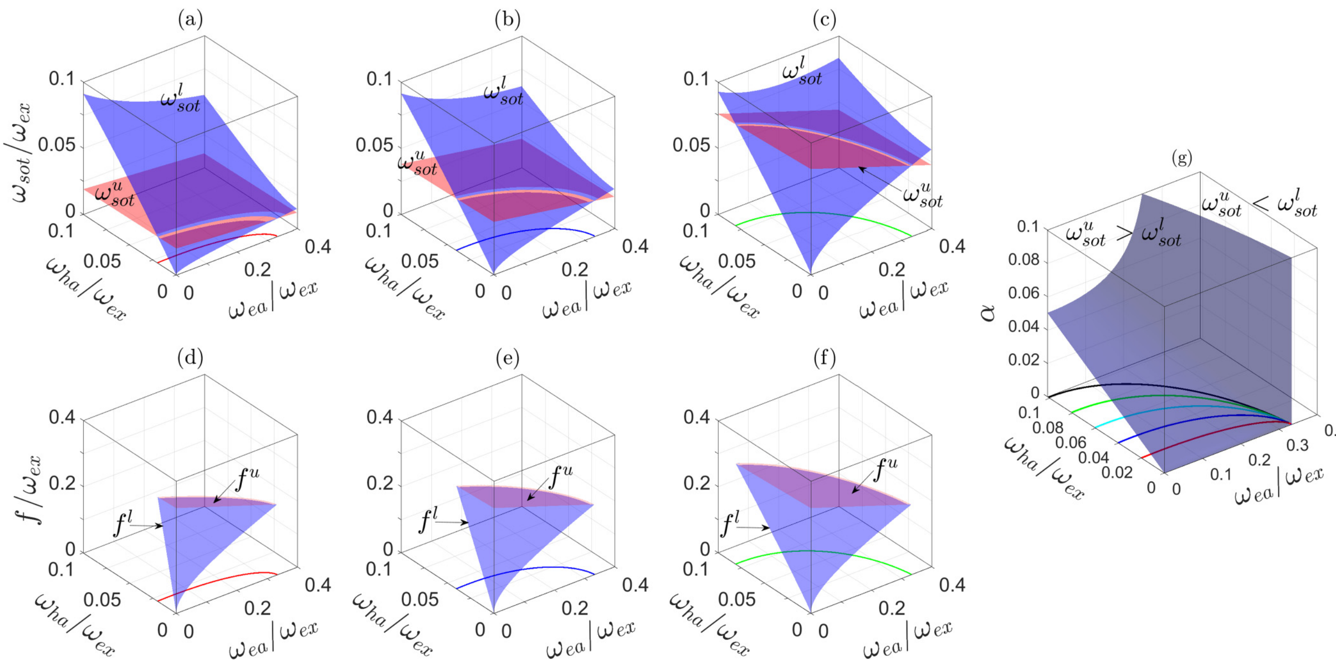

FIG. 3. Range of the self-oscillation for case I. (a), (b), and (c) The lower ($\omega^{l}_{\mathrm{SOT}}$) and upper ($\omega^{u}_{\mathrm{SOT}}$) thresholds of self-oscillations as functions of the easy-axis anisotropy (ω_{ea}) and the hard-axis one (ω_{ha}) for $\alpha = 0.01$, 0.02, and 0.04, respectively. (d), (e), and (f) The frequencies (f^{l} and f^{u}) at the lower and upper thresholds for $\alpha = 0.01$, 0.02, and 0.04, respectively. (g) The isosurface of $\omega^{l}_{\mathrm{SOT}} = \omega^{u}_{\mathrm{SOT}}$. The curves in the ω_{ea}-ω_{ha} plane of (a)–(g) are contours of $\omega^{l}_{\mathrm{SOT}} = \omega^{u}_{\mathrm{SOT}}$. In (g), along the ω_{ha}-axis, the contours correspond to α varying from 0.01 to 0.05 with an increment 0.01.

Second, the easy- and hard-axis anisotropies considerably affect the self-oscillation range. As indicated in Fig. 3, the self-oscillation may appear only in a corner of small ω_{ea} and ω_{ha}. This range can be extended by a heavier damping. As examples, Fig. 4(b) [(c)] shows the dependence of the lower and upper thresholds on ω_{ea} (ω_{ha}), while maintaining ω_{ha} (ω_{ea}) and α unchanged. It can be observed that, for a small ω_{ea} or ω_{ha}, the AFM state is switched to the self-oscillation when increasing ω_{SOT}. With ω_{ea} or ω_{ha} increasing, the adjustable range of ω_{SOT} for the self-oscillation is shrunk. For a large ω_{ea} or ω_{ha} above the critical value determined by $\omega^{l}_{\mathrm{SOT}} = \omega^{u}_{\mathrm{SOT}}$, the SOT flips one sublattice magnetization and compels the system into a FM state, just like magnetic field-driven spin-flip transition [54] in the AFM with a strong anisotropy.

From the condition that $\omega^{l}_{\mathrm{SOT}} < \omega^{u}_{\mathrm{SOT}}$, we can derive that there exists a critical damping constant, only above which the self-oscillation can develop. Namely, $\alpha > \alpha_c$, where

$$\alpha_c = \frac{1}{\sqrt{2}}\frac{1}{2\omega_{\mathrm{ex}} - 2\omega_{\mathrm{ea}} - \omega_{\mathrm{ha}}} \times \sqrt{\sqrt{\frac{2\omega_{\mathrm{ha}}^2\omega_{\mathrm{ex}}(2\omega_{\mathrm{ex}} - 2\omega_{\mathrm{ea}} - \omega_{\mathrm{ha}})^2}{2\omega_{\mathrm{ex}} - 3(2\omega_{\mathrm{ea}} + \omega_{\mathrm{ha}})}} + B^2 - B}, \quad (19)$$

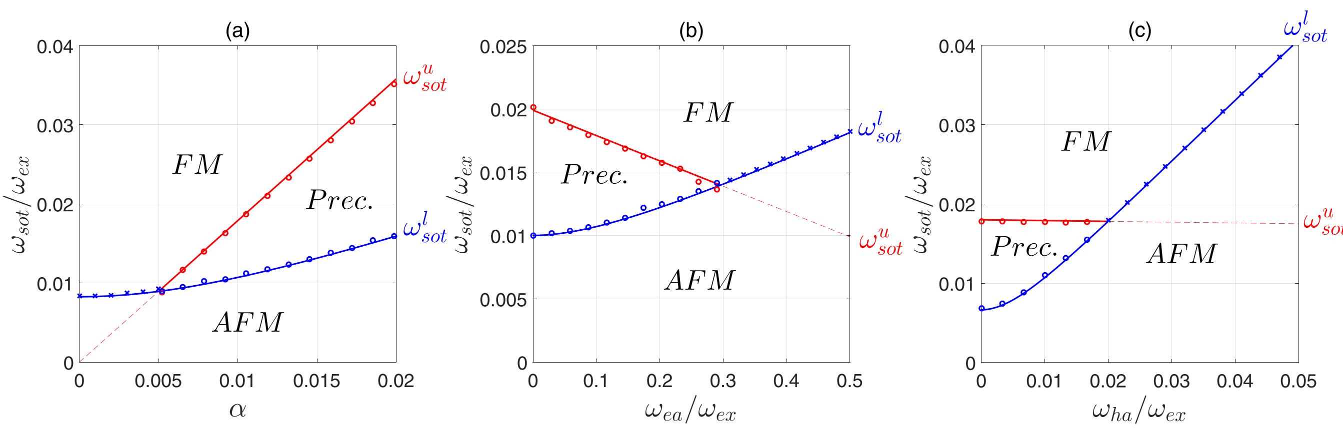

FIG. 4. Phase diagram of case I in the parametric plane spanned by ω_{SOT} and α (a), ω_{SOT} and ω_{ea} (b), as well as ω_{SOT} and ω_{ha} (c). In (a), $\omega_{\mathrm{ea}} = 0.1\omega_{\mathrm{ex}}$ and $\omega_{\mathrm{ha}} = 0.01\omega_{\mathrm{ex}}$. In (b), $\alpha = 0.01$ and $\omega_{\mathrm{ha}} = 0.01\omega_{\mathrm{ex}}$. In (c), $\alpha = 0.01$ and $\omega_{\mathrm{ea}} = 0.1\omega_{\mathrm{ex}}$. The lines correspond to Eqs. (5) and (7). The circles and crosses are plotted by numerically solving Eq. (1) for Case I. "Prec." denotes the precession state, i.e., self-oscillation. The dashed parts of $\omega^{u}_{\mathrm{SOT}}$ curves are not the phase boundaries, just for showing the complete curve of $\omega^{u}_{\mathrm{SOT}}$, i.e., Eq. (7).

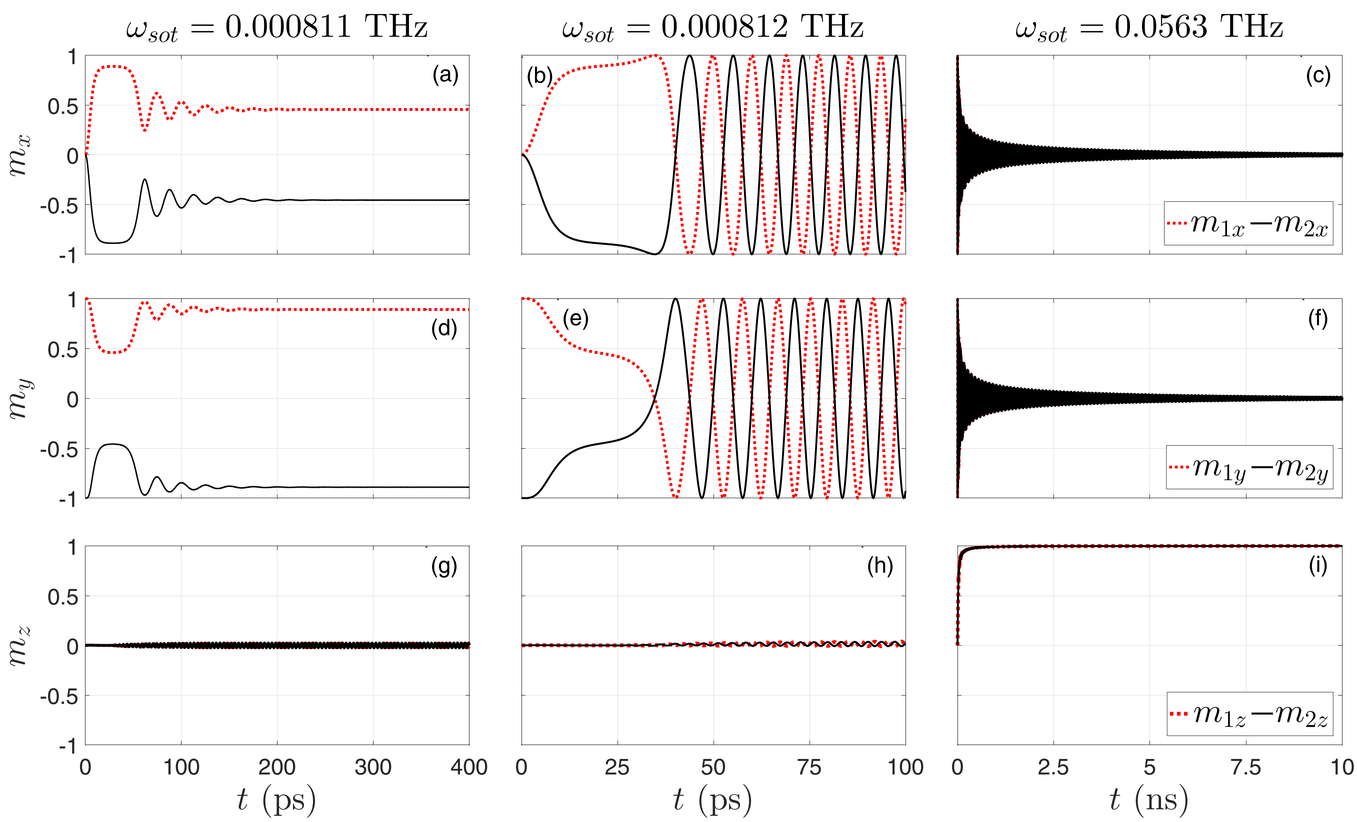

FIG. 5. Evolutions of x-components (upper panel), y-components (middle panel), and z-components (lower panel) of $\mathbf{m}_{1,2}$ for the AFM state (the first column), the precession (the second column), and the FM state (the third column) of case II. The parameters are the same as Fig. 2. Putting them into (21) and (22), the lower and upper thresholds of the self-oscillation are $\omega_{\rm SOT}^{l} = 0.000\,847$ THz and $\omega_{\rm SOT}^{u} = 0.0549$ THz, which is consistent with the numeric results. Here, $\mathbf{m}_1$ ($\mathbf{m}_2$) is initially directed towards the y ($-y$) axis.

with

$$B = (\omega_{\rm ex} + 2\omega_{\rm ea})(\omega_{\rm ex} + 2\omega_{\rm ea} + 2\omega_{\rm ha}). \tag{20}$$

In the absence of the hard-axis anisotropy, $\alpha_c = 0$. The self-oscillation range is independent of the damping. For this case, from $\omega_{\rm SOT}^{l} < \omega_{\rm SOT}^{u}$, we obtain $\omega_{\rm ea} < 1/3\omega_{\rm ex}$. As seen in Fig. 3(g), all the contour lines converge to the point at which $\omega_{\rm ea}/\omega_{\rm ex} = 1/3$. In other words, it $\omega_{\rm ea} > \omega_{\rm ex}/3$, no self-oscillation can arise for any $\omega_{\rm ha}$ and α.

In the absence of the easy-axis anisotropy, the self-oscillation range is related with the damping. Keeping the leading-order terms of α and $\omega_{\rm ha}/\omega_{\rm ex}$, the inequation $\omega_{\rm SOT}^{l} < \omega_{\rm SOT}^{u}$ yields $\omega_{\rm ha} < 2\alpha\omega_{\rm ex}$. As illustrated in Fig. 3(g), the boundary lines are located in different points ($\omega_{\rm ha}/\omega_{\rm ex} \approx 2\alpha$) of the $\omega_{\rm ha}$-axis, which are evenly arrayed according to α.

Finally, let us discuss the range of the frequency. The upper threshold of the frequency (f^u) can be expressed as an analytic equation (18), which is also the resonant frequency of the FM state. In view of the strong exchange, f^u depends weakly on $\omega_{\rm ea}$ and $\omega_{\rm ha}$, as shown by the surfaces marked by f^u in Figs. 3(d), 3(e), and 3(f). On the other hand, it is not possible to obtain analytically the lower threshold of the frequency (f^l). So, we resort to numerically solving Eqs. (17) and (18) with $\omega_{\rm SOT}(\mathcal{E}_n) = \omega_{\rm SOT}^{l}$. Then, we plot the surface of f^l based on the $\omega_{\rm ea}$-$\omega_{\rm ha}$ plane, as shown by the surfaces marked by f^l in Figs. 3(d), 3(e), and 3(f). Inspection of these figures reveals that, unlike f^u, f^l is highly sensitive to the easy- and hard-axis anisotropies. The window of the self-oscillation frequency narrows with the anisotropies increasing.

IV. CASE II: $\mathbf{u}_p \parallel \mathbf{u}_{\rm ha}$

For this case, as shown in Fig. 1, the hard axis ($\mathbf{u}_{\rm ha}$) and the spin polarization ($\mathbf{u}_p$) coincide, assuming they lie along the z direction. The easy axis ($\mathbf{u}_{\rm ea}$) is along the y direction.

A. Lower and upper thresholds of the self-oscillation

By the linear stability analysis or the averaging technique, we now define the stability region of all the stable equilibria, which can be confirmed from numerical integration of the coupled LLGS equations [Eq. (1)] for case II.

Without the SOT, $\mathbf{m}_1$ ($\mathbf{m}_2$) prefers to line up along the y ($-y$) direction. After applying a small SOT, $\mathbf{m}_{1,2}$ are slightly perturbed away from the easy axis, as shown in Figs. 5(a), 5(d), and 5(g). As calculated in Appendix B, $\mathbf{m}_1$ ($\mathbf{m}_2$) rotates in the x-y plane to the direction at an angle of $1/2\arcsin(\omega_{\rm SOT}/\omega_{\rm ea})$ with respect to the y ($-y$) axis. Because $\mathbf{m}_1$ and $\mathbf{m}_2$ still remain antiparallel, this equilibrium is named after a tilted-AFM state, which is stable if $|\omega_{\rm SOT}| < \omega_{\rm SOT}^{l}$, with (see Appendixes B 3 and E for details of the derivation)

$$\omega_{\rm SOT}^{l} = \frac{2\sqrt{\omega_{\rm ea} + \omega_{\rm ha} + \omega_{\rm ex}}\left[\omega_{\rm ea} + 2\alpha\sqrt{\omega_{\rm ea}(\omega_{\rm ha} + \omega_{\rm ex})}\right]}{\pi\sqrt{\omega_{\rm ha} + \omega_{\rm ex}}}. \tag{21}$$

Another stable equilibrium emerges under the large SOT. As demonstrated in Figs. 5(c), 5(f), and 5(i), the large SOT directs $\mathbf{m}_{1,2}$ towards the spin polarization $\mathbf{u}_p$ finally. By the stability analysis, we can infer that $\mathbf{m}_{1,2}$ reach a ferromagnetic saturation when $|\omega_{\rm SOT}| > \omega^u_{\rm SOT}$, where (see Appendix B 2 for details of the derivation)

$$\omega^u_{\rm SOT} = \alpha(2\omega_{\rm ex} + \omega_{\rm ea} + 2\omega_{\rm ha}). \tag{22}$$

There are two other kinds of equilibria, which are unstable for any $\omega_{\rm SOT}$ (see Appendixes B 1 and B 4 for details) and not presented here.

If $\omega^l_{\rm SOT} < \omega^u_{\rm SOT}$, no stable equilibrium exists in the interval in which $\omega^l_{\rm SOT} < |\omega_{\rm SOT}| < \omega^u_{\rm SOT}$. Then, a precessional state may appear, as demonstrated in Figs. 5(b), 5(e), and 5(h).

Below $\omega^l_{\rm SOT}$, a weak SOT tilts $\mathbf{m}_1$ ($\mathbf{m}_2$) from $\mathbf{e}_y$ ($-\mathbf{e}_y$), i.e., the easy axis. Then, driven by the exchange and anisotropy torques, $\mathbf{m}_1$ ($\mathbf{m}_2$) rotates around $\mathbf{e}_y$ ($-\mathbf{e}_y$). Once $\mathbf{m}_1$ and $\mathbf{m}_2$ rotate to the x-y plane, they restore antiparallel. In this scene, the exchange torques vanish. The SOT is balanced by the anisotropy torque, and the system remains a tilted AFM state, as shown in Figs. 5(a), 5(d), and 5(g). In general, under perturbations, $\mathbf{m}_1$ ($\mathbf{m}_2$) rotates around its equilibrium direction with a small amplitude, forming a linear oscillation.

When $|\omega_{\rm SOT}| > \omega^l_{\rm SOT}$, the anisotropy torque cannot balance the SOT, accompanied by an instability of the linear mode. This relative strong SOT tilts both $\mathbf{m}_1$ and $\mathbf{m}_2$ to $\mathbf{e}_z$ ($-\mathbf{e}_z$) for $\omega_{\rm SOT} > \omega^l_{\rm SOT}$ ($\omega_{\rm SOT} < -\omega^l_{\rm SOT}$), bringing about a conic precession (self-oscillation) around $\mathbf{e}_z$ ($-\mathbf{e}_z$) driven by the exchange torques. With $\omega_{\rm SOT}$ increasing, the conic angle becomes smaller.

If $\omega_{\rm SOT} > \omega^u_{\rm SOT}$ ($\omega_{\rm SOT} < -\omega^u_{\rm SOT}$), the self-oscillation disappears, and $\mathbf{m}_{1,2}$ point to $\mathbf{e}_z$ ($-\mathbf{e}_z$) together, as indicated in Figs. 5(c), 5(f), and 5(i).

B. Frequency of the self-oscillation

By a procedure similar to that in Sec. III B, and taking $\mathbf{u}_p = \mathbf{e}_z$, $\mathbf{u}_{\rm ea} = \mathbf{e}_y$, and $\mathbf{u}_{\rm ha} = \mathbf{e}_z$ (see Fig. 1), the coupled LLGS equation (1) is reduced to a single-vector equation (9), just replacing the energy by

$$\mathcal{E}_n = (\omega_{\rm ex} + \omega_{\rm ha})(\mathbf{n}\cdot\mathbf{e}_z)^2 - \omega_{\rm ea}(\mathbf{n}\cdot\mathbf{e}_y)^2. \tag{23}$$

Then, from Eqs. (12)–(14), we can obtain $\omega_{\rm SOT}$ of a self-oscillation in the $\mathcal{E}_n$ orbit (see Appendix D for details of the derivation),

$$\omega_{\rm SOT}(\mathcal{E}_n) = \frac{4\alpha\sqrt{(\omega_{\rm ea}+\mathcal{E}_n)(\omega_{\rm ex}+\omega_{\rm ea}+\omega_{\rm ha})}}{\pi(\omega_{\rm ex}+\omega_{\rm ha}-\mathcal{E}_n)} \times[(\omega_{\rm ex}+\omega_{\rm ha})\mathsf{E}(k) - \mathcal{E}_n\mathsf{K}(k)], \tag{24}$$

where the modulus k of the elliptic integrals reads

$$k = \sqrt{\frac{\omega_{\rm ea}(\omega_{\rm ex}+\omega_{\rm ha}-\mathcal{E}_n)}{(\omega_{\rm ea}+\mathcal{E}_n)(\omega_{\rm ha}+\mathcal{E}_n)}}. \tag{25}$$

The frequency is calculated as (see Appendix D for details of the derivation)

$$f(\mathcal{E}_n) = \frac{\sqrt{\mathcal{E}_n(\omega_{\rm ex}+\omega_{\rm ea}+\omega_{\rm ha})}}{2\mathsf{K}(k)}. \tag{26}$$

Eliminating $\mathcal{E}_n$ from Eqs. (24) and (26), we can calculate the dependence of the frequency on the SOT. At the upper threshold, $\mathcal{E}_n = \omega_{\rm ex} + \omega_{\rm ha}$, and the corresponding frequency

$$f^u = \frac{1}{\pi}\sqrt{(\omega_{\rm ex}+\omega_{\rm ha})(\omega_{\rm ex}+\omega_{\rm ea}+\omega_{\rm ha})}. \tag{27}$$

C. Range of the self-oscillation

Here, from Eqs. (21) and (22), we analyze the dependence of the self-oscillation range of $\omega_{\rm SOT}$ on the damping, the easy-, and hard-axis anisotropies. In addition, the frequency range is inferred from Eqs. (24), (26), and (27).

When a spin current with $\mathbf{u}_p \parallel \mathbf{u}_{\rm ha}$ is injected into the biaxial AFM, the AFM state is disturbed and we observe either a tilted-AFM state or self-oscillations depending on the magnitude of the SOT, as well as the strengthes of the damping and the magnetic anisotropies. First, similar to Case I, the self-oscillation range becomes wider for a heavier damping. Comparing Figs. 5(a), 5(b), and 5(c) reveals that, along with an increasing α, the region of $\omega^l_{\rm SOT} < \omega^u_{\rm SOT}$ expands. Namely, the self-oscillation range is enlarged. This feature is also illustrated in Fig. 7(a), where we plot the lower and upper thresholds as a function of α while keeping $\omega_{\rm ea}$ and $\omega_{\rm ha}$ constant. For a small damping, with an increasing SOT, the system switches directly from the tilted-AFM to the FM state at $\omega^l_{\rm SOT}$. For a large damping, the self-oscillation occurs first. Then, if the SOT increases further, the system enters the FM state at $\omega^u_{\rm SOT}$.

The critical damping constant, beyond which the self-oscillation can then exist, is easily gotten by solving $\omega^l_{\rm SOT} = \omega^u_{\rm SOT}$,

$$\alpha_c = \frac{2}{\pi}\frac{\sqrt{\frac{\omega_{\rm ea}}{\omega_{\rm ex}+\omega_{\rm ha}}}}{\frac{2\omega_{\rm ex}+\omega_{\rm ea}+2\omega_{\rm ha}}{\sqrt{\omega_{\rm ea}}\sqrt{\omega_{\rm ex}+\omega_{\rm ea}+\omega_{\rm ha}}} - \frac{4}{\pi}}. \tag{28}$$

As shown in Fig. 6(g), this critical damping is depicted as an isosurface in the α-$\omega_{\rm ea}$-$\omega_{\rm ha}$ parametric space. Above this surface, the self-oscillation happens when the tilted-AFM state becomes unstable. Below this surface, no self-oscillation occurs and a FM state emerges after an instability of the tilted-AFM state at $\omega^l_{\rm SOT}$.

Second, the influence of anisotropies on the self-oscillation range differs from Case I, as observed by comparing Figs. 3 and 6. In particular, the hard-axis anisotropy enlarges the self-oscillation range, as shown in Fig. 7(c). By contrast, the easy-axis anisotropy shrinks the self-oscillation range, as indicated in Fig. 7(b). In the absence of the easy-axis anisotropy, the lower threshold becomes zero. This means that an infinitesimal current can excite the self-oscillation for this highly symmetric case.

Finally, the frequency range of the self-oscillation is shown in Figs. 6(d), 6(e), and 6(f). It can be observed that the range of frequency becomes wider with increasing $\omega_{\rm ha}$, while it becomes narrower with increasing $\omega_{\rm ea}$. The hard axis $\mathbf{u}_{\rm ha}$ coincides with the spin polarization $\mathbf{u}_p$, which is also the precessional axis. So, the torque of the hard-axis anisotropy $[\omega_{\rm ha}(\mathbf{m}_i\cdot\mathbf{u}_{\rm ha})(\mathbf{m}_i\times\mathbf{u}_{\rm ha})]$ propels the magnetic moments to rotate left-handedly, playing the same role as the exchange torque. Thus, a stronger hard-axis anisotropy favors a wider frequency range.

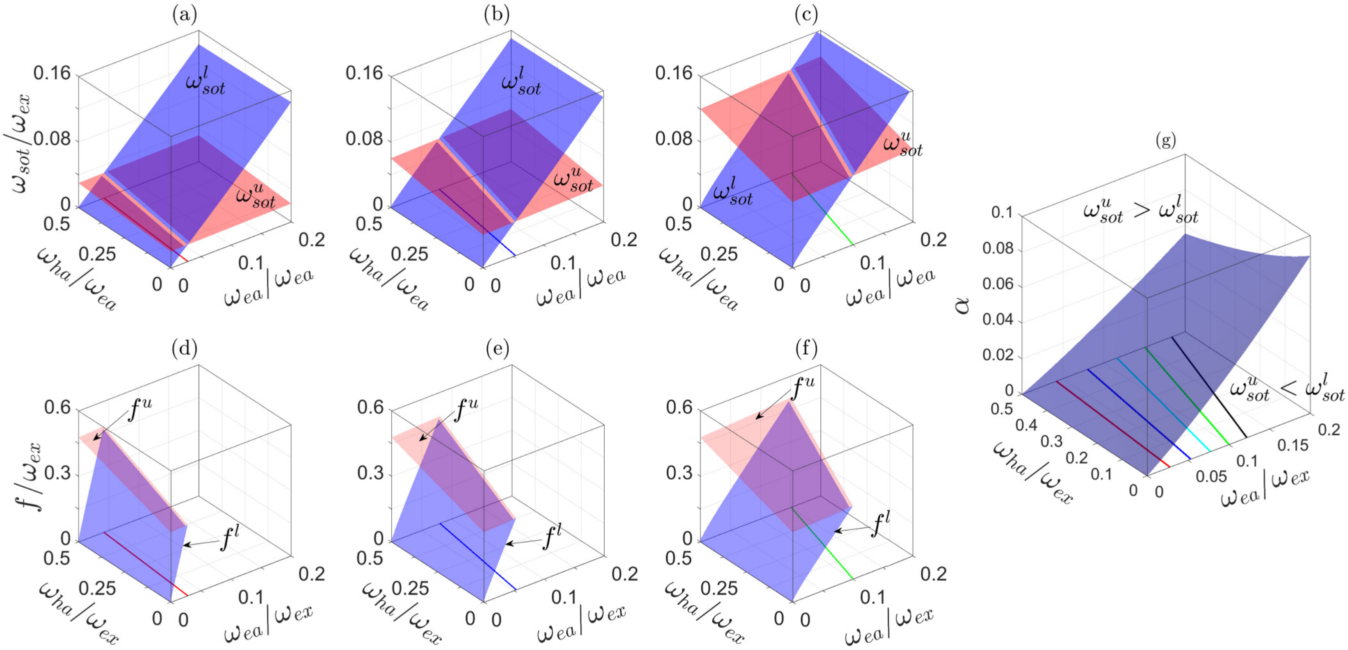

FIG. 6. Range of the self-oscillation for case II. (a), (b), and (c) The lower (ω^l_{SOT}) and upper (ω^u_{SOT}) thresholds of self-oscillations as functions of the easy-axis anisotropy (ω_{ea}) and the hard-axis one (ω_{ha}) for $\alpha = 0.01$, 0.02, and 0.04, respectively. (d), (e), and (f) The frequencies (f^l and f^u) at lower and upper thresholds for $\alpha = 0.01$, 0.02, and 0.04, respectively. (g) The isosurface of $\omega^l_{\mathrm{SOT}} = \omega^u_{\mathrm{SOT}}$. The curves in the ω_{ea}-ω_{ha} plane of (a)–(g) are contours of $\omega^l_{\mathrm{SOT}} = \omega^u_{\mathrm{SOT}}$. In (g), along the ω_{ea}-axis, the contours correspond to α varying from 0.01 to 0.05 with an increment 0.01.

V. DISCUSSION

First, it should be mentioned that the orbits of self-oscillation are located in the upper hemisphere ($m_z > 0$) for $\omega_{\mathrm{SOT}} > 0$, while they are in the lower hemisphere for $\omega_{\mathrm{SOT}} < 0$. Taking into account the similarity of precessions for positive and negative ω_{SOT}, we restrict our discussion to positive ω_{SOT}. Moreover, we only study two special cases with the spin polarization along the easy and hard axes, for which the system is symmetric with respect to the x-z and y-z planes. Combining this symmetry with the evolutions of $\mathbf{m}_{1,2}$, we reduce the coupled LLGS equations to a single-vector one, which can be treated analytically by the averaging technique. The analytic expressions are verified by comparing with numerical results by solving the original LLGS equations numerically. However, difficulties arise when an attempt is made to generalize this method to arbitrary spin polarizations [33,56,57]. Although we do not consider arbitrary spin polarizations, a further investigation about this case may be valuable.

Second, to show flexibility in SOT control of the AFM self-oscillations, we do not select parameters that correspond precisely to a specific AFM in analyzing the ranges of the frequency and the strength of SOT. However, it is instrumental to calculate the values of the frequency and the exciting current

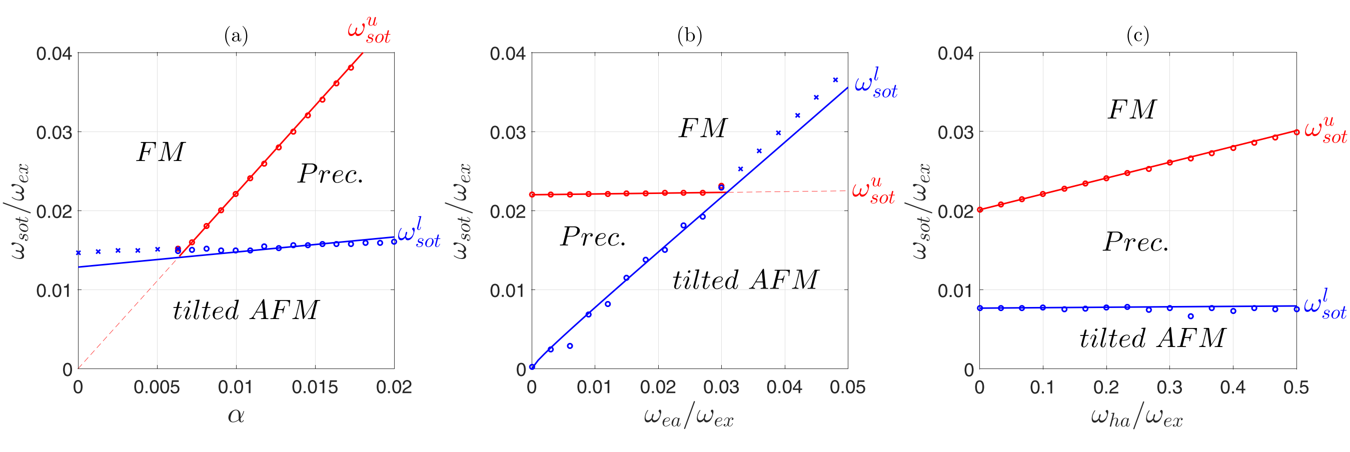

FIG. 7. Phase diagram of case II in the parametric plane spanned by ω_{SOT} and α (a), ω_{SOT} and ω_{ea} (b), as well as ω_{SOT} and ω_{ha} (c). In (a), $\omega_{\mathrm{ea}} = 0.02\omega_{\mathrm{ex}}$ and $\omega_{\mathrm{ha}} = 0.1\omega_{\mathrm{ex}}$. In (b), $\alpha = 0.01$ and $\omega_{\mathrm{ha}} = 0.1\omega_{\mathrm{ex}}$. In (c), $\alpha = 0.01$ and $\omega_{\mathrm{ea}} = 0.01\omega_{\mathrm{ex}}$. The lines correspond to Eqs. (21) and (22). The circles and crosses are plotted by numerically solving Eq. (1) for Case II. "Prec." denotes the precession state, i.e., self-oscillation. The dashed parts of ω^l_{SOT} curves are not the phase boundaries, just showing the complete curve of ω^u_{SOT}, i.e., Eq. (22).

TABLE I. Magnetic parameters of several typical AFMs and their self-oscillation thresholds of the current and frequency. For Case I, the current thresholds are calculated from Eqs. (4), (5), and (7), and the frequency thresholds from Eqs. (5), (15), (17), and (18). For Case II, the current thresholds are calculated from Eqs. (4), (21), and (22), and the frequency thresholds are calculated from Eqs. (21), (24), (26), and (27). The values in the parentheses are obtained by solving the LLGS equation [Eq. (1)] numerically. The critical damping constants are calculated from Eq. (19) for Case I, and Eq. (28) for Case II. For all listed AFMs, the SOT efficiency $\xi = 0.1$, the damping constant $\alpha = 0.001$, and the thickness of the AFM layer $d = 4$ nm.

	Magnetic parameters				Current and frequency thresholds of self-oscillations: Case I: $\mathbf{u}_p \parallel \mathbf{u}_{\rm ea}$ ($\mathbf{u}_p \perp \mathbf{u}_{\rm ha}$)					Case II: $\mathbf{u}_p \parallel \mathbf{u}_{\rm ha}$ ($\mathbf{u}_p \perp \mathbf{u}_{\rm ea}$)				
	$\omega_{\rm ex}$ (THz)	$\omega_{\rm ea}$ (GHz)	$\omega_{\rm ha}$ (GHz)	M_s (kA/m)	α_c	j_e^l (TA/m^2)	j_e^u (TA/m^2)	f^l (THz)	f^u (THz)	α_c	j_e^l (TA/m^2)	j_e^u (TA/m^2)	f^l (THz)	f^u (THz)
NiO[a]	27.4	1	23	351	0.00042	5.58 (5.60)	13.3 (13.6)	3.66 (3.72)	8.72 (8.33)	0.000012	0.206 (0.197)	13.3 (13.7)	0.135 (0.124)	8.73 (8.62)
MnF_2[b]	7.79	136	0	47.7	0	0.0684 (0.0689)	0.505 (0.554)	0.331 (0.331)	2.436 (2.439)	0.0061	2.92	0.52		
Cr_2O_3[c]	42.4	12	0	286	0	0.282 (0.280)	16.8 (17.1)	0.226 (0.227)	13.5 (12.5)	0.000091	1.69 (1.80)	16.8 (17.2)	1.36 (1.46)	13.5 (13.5)
MnPt[d]	30.5	0	387	632	0.0063	167	26.5			0	0	27.0 (27.5)	0	9.83 (9.71)

[a]References [24,25,52,53].
[b]References [58–61].
[c]References [62,63].
[d]References [64–68].

for some typical AFM materials. The preceding calculations are also suitable for the uniaxial AFMs, including the easy-axis and easy-plane types. Then, in Table I, taking the biaxial (NiO), easy-axis (MnF_2 and Cr_2O_3), and easy-plane (MnPt) AFMs as examples, we list the lower and upper thresholds of electric currents and the corresponding frequencies for the two cases. For comparison, except for the magnetic parameters, the damping constant, the SOT efficiency, and the thickness of the AFM layer take the same values. In particular, we plot the frequency as a function of the current density in Fig. 8 for the biaxial NiO.

From Table I and Fig. 8, several conclusions are immediately seen. (i) The frequency lies in the range of THz and increases with the current nearly linearly. (ii) For a biaxial AFM (NiO), the current and frequency ranges of Case II are wider than those of Case I. However, the opposite happens for an easy-axis AFM (Cr_2O_3). This is related to the role of hard-axis anisotropy on the self-oscillation. In the absence of a hard axis (such as Cr_2O_3), until the SOT tilts $\mathbf{m}_{1,2}$ from the antiparallel state enough, the exchange torques between $\mathbf{m}_1$ and $\mathbf{m}_2$ propel them to rotate around the spin-polarization direction ($\mathbf{u}_p$). In the presence of a hard axis (for example, NiO), if $\mathbf{u}_p$ coincides with the hard axis (namely, for Case II), the hard-axis anisotropy torque drives $\mathbf{m}_{1,2}$ precessing left-handedly, just like the exchange torque. But, the tilting of $\mathbf{m}_{1,2}$ is not required. Even for an antiparallel state, $\mathbf{m}_{1,2}$ can precess around the hard axis. Thus, the self-oscillation occurs just for a slight tilting of $\mathbf{m}_{1,2}$, which results in a smaller lower threshold. (iii) For easy-axis AFMs, the critical damping constant (α_c) vanishes for Case I. For easy-plane AFMs, α_c vanishes for Case II. (iv) When $\alpha < \alpha_c$, the lower current threshold (j_e^l) is greater than the upper one (j_e^u), as shown in Table I for Case I of MnPt and Case II of MnF_2. So, the self-oscillation window is closed for this scenario. As argued in Secs. III C and IV C, the system flips from an AFM state to a FM at the lower threshold.

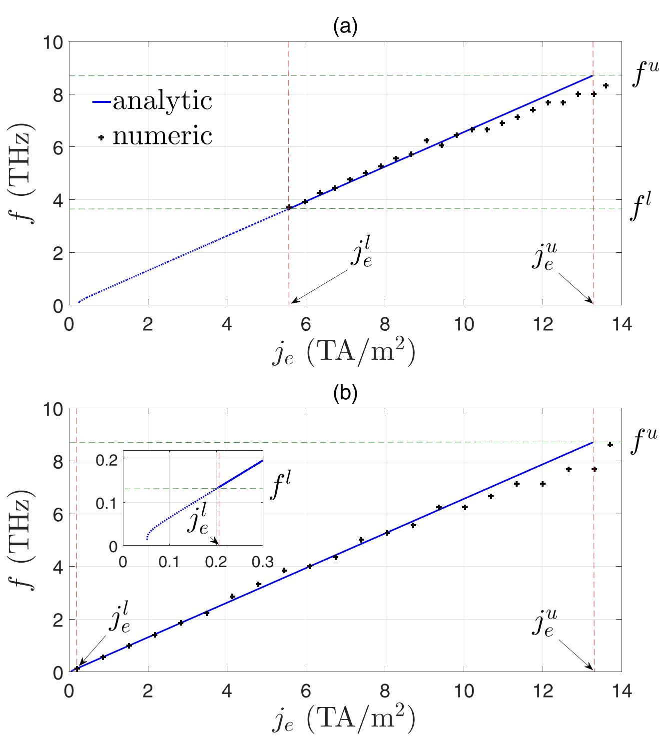

FIG. 8. The dependance of frequency on the current density for Case I (a) and Case II (b). The magnetic parameters of NiO are adopted. Other parameters are the same as Table I. The inset shows magnified views around the lower threshold for Case II. The dotted lines are analytic results, of which the corresponding self-oscillations are unstable.

Third, we discuss the possible approaches to detect the self-oscillations, during which $m_{1x} = -m_{2x}$, $m_{1y} = -m_{2y}$, and $m_{1z} = m_{2z}$ remain, and the z-components are almost constant. As such, for methods based on the spin Hall magnetoresistance [46,69] and the inverse spin Hall effect combining with the spin pumping [24,25], of which the output signals depend on $\sum_i(\mathbf{m}_i \cdot \mathbf{u}_p)^2$ $(=m_{1z}^2 + m_{2z}^2)$ [46], it is difficult to generate detectable ac signals.

Fortunately, the anisotropic magnetoresistance (AMR) [46,70] depends on the angle between the electric current and the magnetization direction, $\sim \sum_i(\mathbf{m}_i \cdot \mathbf{j}_c)^2$ [46]. Then, an ac signal can be extracted from the THz oscillations of sublattice magnetizations. In view of the periodic variation of the angle between $\mathbf{m}_{1,2}$ and the current $\mathbf{j}_e$, two electrodes can be attached on end points of the metallic AFM layer to probe the self-oscillation. Because the detecting current mostly passes through the AFM layer, it barely affects the longitudinal current in the HM layer, which induces the SOT via the spin Hall effect. Hence, in the single-domain formalism, the detecting current cannot influence the magnetic dynamics driven by the SOT. Furthermore, to avoid the influence of the detecting current on the dynamics, it is useful to add a capacitor on the probing branch circuit and a solenoid on the input dc one.

On the other hand, for the insulating AFM/HM bilayer structures, tunneling AMR may be a choice to probe the self-oscillations. It has been proposed [71] and realized [72] that the AFM dynamics can be detected by the measured tunneling AMR in the FM/metallic AFM/insulator/HM spin-valve structures. A similar scheme has been put forward to produce a THz signal in a Pt/metallic AFM/MgO/Pt structure [73]. Besides, it has been revealed that [74], in a junction composed by a ferromagnetic insulating barrier sandwiched between nonmagnetic electrodes, there is a remarkable angular dependence of the tunneling AMR. Here, the magnetization direction in the magnetic insulating barrier affects the resistance. A similar effect has been found in a multilayer based on an AFM barrier [75], where switching of the AFM order parameter in the barrier leads to a substantial change of the resistance of the junction. Inspired by these works, it is natural to conjecture that the AFM self-oscillation does influence the tunneling current through it, generating an ac signal via the tunneling AMR in the nonmagnetic electrode/insulating AFM/HM structure.

Finally, it is worth mentioning that the effective damping constant is determined by the spin pumping mechanism, and it relies on the thickness of the AFM layer [25]. Moreover, the anisotropy constant can be controlled by a voltage [76,77]. Therefore, besides choosing different AFMs, the damping and anisotropy constants may be adjusted even for a particular AFM.

VI. CONCLUSION

In conclusion, for the AFMs driven by a dampinglike SOT with the spin polarization along the easy axis (case I) or the hard axis (case II), we analytically formulate the lower and upper thresholds of self-oscillations by the linear stability analysis or the average technique. Additionally, we derive the dependence of the self-oscillation frequency on the strength of SOT.

Based on these analytic results, we analyze the influences of the damping and the easy- and hard-axis anisotropies on the adjustable range of a self-oscillation. We find that enhancing the damping can expand the adjustable range of the current and the frequency. This is because a stable self-oscillation is sustained by the balance between the dampinglike SOT and the damping. Along with the damping increasing, the SOT also increases to oppose the damping. This results in an expanding of the adjustable range. Moreover, there exists a critical damping, only beyond which the self-oscillation can occur. If the system is axial symmetry, for example, $\omega_{\mathrm{ha}} = 0$ for case I and $\omega_{\mathrm{ea}} = 0$ for case II, this critical damping vanishes. Also, $\omega_{\mathrm{SOT}}^l = 0$, i.e., an infinitesimal current can generate a self-oscillation. In addition, the adjustable range shrinks with ω_{ea} and ω_{ha} increasing for case I, while for case II, it shrinks with ω_{ea} increasing, and broadens with ω_{ha} increasing.

Next, by changing the values of damping and anisotropies, we discover that there exist two kinds of transitions of the magnetic states when increasing the current. For both cases, an AFM-FM transition can happen for a weak damping, similar to the spin-flip transition [54] of AFMs with a strong anisotropy under an increasing magnetic field. For a heavy damping, the AFM state is switched to the self-oscillation with the current increasing. For case I, the spin-flip transition occurs for large easy-axis and hard-axis anisotropies, while the transition from AFM to self-oscillation occurs for small ones. For case II, which transition happens is determined by the easy-axis anisotropy.

AFM materials are more abundant than FMs [46]. There are more choices of the magnetic parameters, such as the damping constant, and the easy-axis and hard-axis anisotropy constants. Moreover, these parameters can be tuned in experiment for one AFM. These offer a possibility to adjust the AFM oscillators over a broad frequency range for realistic material parameters and electric currents. So, it can be expected that our results can not only enrich the current-driven nonlinear magnetic dynamics, but also serve as a guideline to design the THz AFM oscillators.

ACKNOWLEDGMENTS

This work was supported by the National Natural Science Foundation of China (Grants No. 51972103 and No. 21938002).

APPENDIX A: EQUILIBRIA AND THEIR STABILITIES FOR CASE I

In this case, the spin polarization is along the easy axis. So, we can take $\mathbf{u}_p = \mathbf{u}_{\mathrm{ea}} = \mathbf{e}_z$ and $\mathbf{u}_{\mathrm{ha}} = \mathbf{e}_x$, as shown in Fig. 1. The equilibria are obtained when the SOT balances out the precessional torques, i.e.,

$$\mathbf{m}_i \times \frac{d\mathcal{E}}{d\mathbf{m}_i} = \omega_{\mathrm{SOT}} \mathbf{m}_i \times (\mathbf{m}_i \times \mathbf{u}_p). \tag{A1}$$

To solve these equilibrium equations (A1), it is convenient to parametrize the unit magnetization vectors $\mathbf{m}_i$ in terms of the polar angle θ_i and the azimuthal one ϕ_i according to $\mathbf{m}_i = (\sin\theta_i\cos\phi_i, \sin\theta_i\sin\phi_i, \cos\theta_i)$. Then, one has

$$\begin{aligned}\left(\omega_{\rm SOT} - \omega_{\rm ha}\sin 2\phi_i^0\right)\sin\theta_i^0\\ = \omega_{\rm ex}\sin\left(\phi_i^0 - \phi_{3-i}^0\right)\sin\theta_{3-i}^0,\end{aligned} \tag{A2}$$

$$\begin{aligned}\left[\omega_{\rm ex}\cos\theta_{3-i}^0 - 2\left(\omega_{\rm ea} + \omega_{\rm ha}\cos^2\phi_i^0\right)\cos\theta_i^0\right]\sin\theta_i^0\\ = \omega_{\rm ex}\cos\left(\phi_i^0 - \phi_{3-i}^0\right)\cos\theta_i^0\sin\theta_{3-i}^0.\end{aligned} \tag{A3}$$

Obviously, $\theta_i^0 = 0$ or π solves Eqs. (A2) and (A3), generating two FM states. Similarly, $\theta_1^0 = 0\,(\pi)$ and $\theta_2^0 = \pi\ (0)$ compose the AFM states.

For $\sin\theta_i^0 \neq 0$, there exist other kinds of solutions, which satisfy $\sin 2\phi_i^0 = \omega_{\rm SOT}/\omega_{\rm ha}$, $\sin(\phi_1^0 - \phi_2^0) = 0$, and $\cos\theta_i^0 = 0$. These yield four FM states in which $\theta_i^0 = \pi/2$ and $\phi_i^0 = \phi^0$, and four AFM states in which $\theta_i = \pi/2$, $\phi_1^0 = \phi^0$, and $\phi_2^0 = \pi - \phi^0$. ϕ^0 reads

$$\phi^0 = \frac{1}{2}\left[(P-1)\pi - (-1)^P \arcsin\frac{\omega_{\rm SOT}}{\omega_{\rm ha}}\right], \tag{A4}$$

with $P = 1, 2, 3, 4$. For these two kinds of equilibria, $\mathbf{m}_i$ are located in the x-y plane and deviate from the easy axis. So, we name them tilted-FM or tilted-AFM states. In the following, we will derive the stable regions of the above four kinds of equilibria by the linear stability analysis.

1. Stability analysis of AFM states

For these states, $\theta_1^0 = 0\,(\pi)$ and $\theta_2^0 = \pi\ (0)$. In the spherical coordinate system, these equilibria are two singular points, because ϕ_i^0 is not defined. So, we use the Cartesian coordinate instead, in which the equilibria are expressed as $\mathbf{m}_1^0 = \eta\mathbf{e}_z$ and $\mathbf{m}_2^0 = -\eta\mathbf{e}_z$ with $\eta = \pm 1$. Under a small perturbation, the magnetic moments deviate from the equilibria slightly, i.e., $\mathbf{m}_i = \mathbf{m}_i^0 + \delta m_{ix}\mathbf{e}_x + \delta m_{iy}\mathbf{e}_y$, with δm_{ix} and δm_{iy} being the responses to the perturbation.

To linearize Eq. (1) in the vicinity of these equilibria, we rewrite it in the component form. Considering the constraint of unit norm for $\mathbf{m}_{1,2}$, we only need to use the x- and y-component equations, which read

$$\dot{m}_{ix} - \alpha(m_{iy}\dot{m}_{iz} - m_{iz}\dot{m}_{iy}) = f_i^x, \tag{A5}$$

$$\dot{m}_{iy} - \alpha(m_{iz}\dot{m}_{ix} - m_{ix}\dot{m}_{iz}) = f_i^y, \tag{A6}$$

where the dot convention for the time derivative has been adopted, and

$$\begin{aligned}f_i^x = \omega_{\rm ex}(m_{iy}m_{(3-i)z} - m_{iz}m_{(3-i)y})\\ - 2\omega_{\rm ea}m_{iy}m_{iz} - \omega_{\rm SOT}m_{iz}m_{ix},\end{aligned} \tag{A7}$$

$$\begin{aligned}f_i^y = \omega_{\rm ex}(m_{iz}m_{(3-i)x} - m_{ix}m_{(3-i)z})\\ - 2(\omega_{\rm ea} + \omega_{\rm ha})m_{iz}m_{ix} - \omega_{\rm SOT}m_{iy}m_{iz}.\end{aligned} \tag{A8}$$

By use of $m_{ix}^2 + m_{iy}^2 + m_{iz}^2 = 1$, the z-component equations can be obtained from Eqs. (A5)–(A8).

Inserting the ansatz $\mathbf{m}_i = \mathbf{m}_i^0 + \delta m_{ix}\mathbf{e}_x + \delta m_{iy}\mathbf{e}_y$ into Eqs. (A5)–(A8) and keeping the linear terms of δm_{ix} and δm_{iy}, the obtained linearized system near the equilibria is governed by

$$\mathcal{A}\dot{\mathbf{x}} = \mathcal{B}\mathbf{x}, \tag{A9}$$

where $\mathbf{x} = (\delta m_{1x}, \delta m_{1y}, \delta m_{2x}, \delta m_{2y})^T$, with T denoting the matrix transpose,

$$\mathcal{A} = \begin{pmatrix} 1 & \eta\alpha & 0 & 0\\ -\eta\alpha & 1 & 0 & 0\\ 0 & 0 & 1 & \eta\alpha\\ 0 & 0 & -\eta\alpha & 1\end{pmatrix}, \tag{A10}$$

and $\mathcal{B}$ is the Jacobian matrix at the equilibrium,

$$\mathcal{B} = \begin{pmatrix} \frac{\partial f_1^x}{\partial m_{1x}} & \frac{\partial f_1^x}{\partial m_{1y}} & \frac{\partial f_1^x}{\partial m_{2x}} & \frac{\partial f_1^x}{\partial m_{2y}}\\ \frac{\partial f_1^y}{\partial m_{1x}} & \frac{\partial f_1^y}{\partial m_{1y}} & \frac{\partial f_1^y}{\partial m_{2x}} & \frac{\partial f_1^y}{\partial m_{2y}}\\ \frac{\partial f_2^x}{\partial m_{1x}} & \frac{\partial f_2^x}{\partial m_{1y}} & \frac{\partial f_2^x}{\partial m_{2x}} & \frac{\partial f_2^x}{\partial m_{2y}}\\ \frac{\partial f_2^y}{\partial m_{1x}} & \frac{\partial f_2^y}{\partial m_{1y}} & \frac{\partial f_2^y}{\partial m_{2x}} & \frac{\partial f_2^y}{\partial m_{2y}} \end{pmatrix}_{\mathbf{m}_i = \mathbf{m}_i^0}. \tag{A11}$$

Then, taking the oscillating ansatz ($\delta m_{ix}, \delta m_{iy} \propto e^{\lambda t}$) into Eq. (A9), the existence of a nontrivial solution leads to the secular equation

$$a_0\lambda^4 + a_1\lambda^3 + a_2\lambda^2 + a_3\lambda + a_4 = 0, \tag{A12}$$

where

$$a_0 = (1+\alpha^2)^2, \tag{A13}$$

$$a_1 = 4\alpha(1+\alpha^2)(\omega_{\rm ex} + 2\omega_{\rm ea} + \omega_{\rm ha}), \tag{A14}$$

$$\begin{aligned}a_2 = 2\big\{2[(2\omega_{\rm ea} + \omega_{\rm ha})\omega_{\rm ex} + 2\omega_{\rm ea}(\omega_{\rm ea} + \omega_{\rm ha})]\\ + 2\alpha^2\big[\omega_{\rm ex}^2 + 3(2\omega_{\rm ea} + \omega_{\rm ha})\omega_{\rm ex} + 6\omega_{\rm ea}^2\\ + 6\omega_{\rm ea}\omega_{\rm ha} + \omega_{\rm ha}^2\big] - (1-\alpha^2)\omega_{\rm SOT}^2\big\},\end{aligned} \tag{A15}$$

$$\begin{aligned}a_3 = 4\alpha(\omega_{\rm ex} + 2\omega_{\rm ea} + \omega_{\rm ha})\big[4\omega_{\rm ea}(\omega_{\rm ea} + \omega_{\rm ha})\\ + 2(2\omega_{\rm ea} + \omega_{\rm ha})\omega_{\rm ex} + \omega_{\rm SOT}^2\big],\end{aligned} \tag{A16}$$

$$\begin{aligned}a_4 = \big[4\omega_{\rm ea}(\omega_{\rm ea} + \omega_{\rm ha}) + \omega_{\rm SOT}^2\big]\big[4(\omega_{\rm ex} + \omega_{\rm ea})\\ \times(\omega_{\rm ex} + \omega_{\rm ea} + \omega_{\rm ha}) + \omega_{\rm SOT}^2\big].\end{aligned} \tag{A17}$$

It should be noted that the secular equation is independent of η. This is due to the equivalence of the two AFM states.

If all the roots of λ have a negative real part, the corresponding equilibrium state is stable. This can be judged by the Routh-Hurwitz criterion [78–80], which defines a series of determinants,

$$\Delta_1 = a_1, \tag{A18}$$

$$\Delta_2 = \begin{vmatrix} a_1 & a_0\\ a_3 & a_2\end{vmatrix}, \tag{A19}$$

$$\Delta_3 = \begin{vmatrix} a_1 & a_0 & 0\\ a_3 & a_2 & a_1\\ 0 & a_4 & a_3\end{vmatrix}, \tag{A20}$$

$$\Delta_4 = a_4\Delta_3. \tag{A21}$$

If all Δ are positive, the real parts of all roots of λ are negative. Namely, this equilibrium state is stable.

Inserting Eqs. (A13)–(A17) into Eqs. (A18)–(A21), the Routh-Hurwitz determinants for the AFM states read

$$\Delta_1 = 4\alpha(1+\alpha^2)(\omega_{\rm ex}+2\omega_{\rm ea}+\omega_{\rm ha}), \tag{A22}$$

$$\begin{aligned}\Delta_2 = \Delta_1\big\{&2[(2\omega_{\rm ea}+\omega_{\rm ha})\omega_{\rm ex}+2\omega_{\rm ea}(\omega_{\rm ea}+\omega_{\rm ha})]\\ &+2\alpha^2\big[2\omega_{\rm ex}^2+5(2\omega_{\rm ea}+\omega_{\rm ha})\omega_{\rm ex}\\ &+2\big(5\omega_{\rm ea}^2+5\omega_{\rm ea}\omega_{\rm ha}+\omega_{\rm ha}^2\big)\big]\\ &-(3-\alpha^2)\omega_{\rm SOT}^2\big\},\end{aligned} \tag{A23}$$

$$\begin{aligned}\Delta_3 = \frac{\Delta_1^2}{1+\alpha^2}\big\{&4\omega_{\rm ha}^2\omega_{\rm ex}^2+4\big[\alpha^2(2\omega_{\rm ea}+\omega_{\rm ha})\\ &\times(2\omega_{\rm ex}+2\omega_{\rm ea}+\omega_{\rm ha})-\omega_{\rm SOT}^2\big]\big[(\omega_{\rm ex}+2\omega_{\rm ea})\\ &\times(\omega_{\rm ex}+2\omega_{\rm ea}+2\omega_{\rm ha})+\omega_{\rm SOT}^2\big]\big\},\end{aligned} \tag{A24}$$

$$\Delta_4 = a_4\Delta_3. \tag{A25}$$

It is apparent that $a_4 > 0$ and $\Delta_1 > 0$. Thus, the stability conditions are simplified as $\Delta_2 > 0$ and $\Delta_3 > 0$.

In view of $\alpha^2 \ll 1$, it can be inferred from $\Delta_2 > 0$ that $|\omega_{\rm SOT}| < \omega_{\rm SOT}^a$, where

$$\begin{aligned}\omega_{\rm SOT}^a = \frac{\sqrt{2}}{\sqrt{3-\alpha^2}}\big\{&[(2\omega_{\rm ea}+\omega_{\rm ha})\omega_{\rm ex}+2\omega_{\rm ea}(\omega_{\rm ea}+\omega_{\rm ha})]\\ &+\alpha^2\big[2\omega_{\rm ex}^2+5(2\omega_{\rm ea}+\omega_{\rm ha})\omega_{\rm ex}\\ &+2\big(5\omega_{\rm ea}^2+5\omega_{\rm ea}\omega_{\rm ha}+\omega_{\rm ha}^2\big)\big]\big\}^{1/2}.\end{aligned} \tag{A26}$$

To solve $\Delta_3 > 0$, we rewrite it as

$$\Delta_3 = -\frac{\Delta_1^2}{1+\alpha^2}\big(\omega_{\rm SOT}^2-r_+\big)\big(\omega_{\rm SOT}^2-r_-\big), \tag{A27}$$

where

$$r_\pm = \tfrac{1}{2}\Big(\pm\sqrt{4\omega_{\rm ha}^2\omega_{\rm ex}^2+A_+^2}-A_-\Big), \tag{A28}$$

with

$$\begin{aligned}A_\pm = &(\omega_{\rm ex}+2\omega_{\rm ea})(\omega_{\rm ex}+2\omega_{\rm ea}+2\omega_{\rm ha})\\ &\pm\alpha^2(2\omega_{\rm ea}+\omega_{\rm ha})(2\omega_{\rm ex}+2\omega_{\rm ea}+\omega_{\rm ha}).\end{aligned} \tag{A29}$$

Given the strong exchange and the small damping, $\omega_{\rm ex} > \omega_{\rm ea(ha)}$ and $\alpha^2 \ll 1$. Then, $A_+ > A_- > 0$ and $r_- < 0 < r_+$. Therefore, the solution of $\Delta_3 > 0$ is $|\omega_{\rm SOT}| < \omega_{\rm SOT}^b$, with $\omega_{\rm SOT}^b = \sqrt{r_+}$.

Combining the solutions of $\Delta_2 > 0$ and $\Delta_3 > 0$, the stability condition is $|\omega_{\rm SOT}| < \min(\omega_{\rm SOT}^a, \omega_{\rm SOT}^b)$. By rearranging terms and squaring, it can be proved that $\omega_{\rm SOT}^a > \omega_{\rm SOT}^b$ by a straightforward derivation. Finally, we conclude that these two equivalent AFM states are stable under the condition that $|\omega_{\rm SOT}| < \omega_{\rm SOT}^l$, where

$$\omega_{\rm SOT}^l = \frac{1}{\sqrt{2}}\sqrt{\sqrt{4\omega_{\rm ha}^2\omega_{\rm ex}^2+A_+^2}-A_-}. \tag{A30}$$

2. Stability analysis of FM states

For these states, $\theta_i^0 = 0$ or π, in a Cartesian coordinate system, corresponding to $\mathbf{m}_i^0 = \eta\mathbf{e}_z$ with $\eta = \pm 1$. By the same procedure as that in Appendix A 1, the secular equation is derived as

$$(a_0\lambda^2+a_1\lambda+a_2)(a_0\lambda^2+a_1\lambda+a_2) = 0, \tag{A31}$$

where

$$a_0 = 1+\alpha^2, \tag{A32}$$

$$a_1 = 2[\alpha(2\omega_{\rm ea}+\omega_{\rm ha})+\eta\omega_{\rm SOT}], \tag{A33}$$

$$a_2 = 4\omega_{\rm ea}(\omega_{\rm ea}+\omega_{\rm ha})+\omega_{\rm SOT}^2, \tag{A34}$$

$$b_0 = 1+\alpha^2, \tag{A35}$$

$$b_1 = 2[-\alpha(2\omega_{\rm ex}-2\omega_{\rm ea}-\omega_{\rm ha})+\eta\omega_{\rm SOT}], \tag{A36}$$

$$b_2 = 4(\omega_{\rm ex}-\omega_{\rm ea})(\omega_{\rm ex}-\omega_{\rm ea}-\omega_{\rm ha})+\omega_{\rm SOT}^2. \tag{A37}$$

In light of the Routh-Hurwitz criterion [78–80], if a_1, a_2, b_1, and b_2 are all positive, the equilibrium state is stable. For a realistic AFM, the exchange coupling is generally stronger than the anisotropy. So, it is reasonable to assume that $\omega_{\rm ex} > \omega_{\rm ea}+\omega_{\rm ha}$. Then, it is obvious that $a_2 > 0$ and $b_2 > 0$. Solving $a_1 > 0$ and $b_1 > 0$ yields $\eta\omega_{\rm SOT} > \max[-\alpha(2\omega_{\rm ea}+\omega_{\rm ha}), \alpha(2\omega_{\rm ex}-2\omega_{\rm ea}-\omega_{\rm ha})]$. Finally, the FM state with $\mathbf{m}_i^0 = \mathbf{e}_z$ is stable if $\omega_{\rm SOT} > \omega_{\rm SOT}^u$, while $\omega_{\rm SOT} < -\omega_{\rm SOT}^u$ is the stable condition of the FM state with $\mathbf{m}_i^0 = -\mathbf{e}_z$. The critical value is

$$\omega_{\rm SOT}^u = \alpha(2\omega_{\rm ex}-2\omega_{\rm ea}-\omega_{\rm ha}). \tag{A38}$$

3. Stability analysis of tilted-AFM states

For these kinds of states, $\theta_{1,2}^0 = \pi/2$, $\phi_1^0 = \phi^0$, and $\phi_2^0 = \pm\pi+\phi^0$, with ϕ^0 being Eq. (A4). To linearize Eq. (1) in the vicinity of these equilibria, we express it in the spherical coordinates

$$\dot{\theta}_i+\alpha\sin\theta_i\dot{\phi}_i = f_i^\theta, \tag{A39}$$

$$-\alpha\dot{\theta}_i+\sin\theta_i\dot{\phi}_i = f_i^\phi, \tag{A40}$$

where

$$\begin{aligned}f_i^\theta = &\,\omega_{\rm ex}\sin\theta_{3-i}\sin(\phi_i-\phi_{3-i})\\ &+\omega_{\rm ha}\sin\theta_i\sin 2\phi_i-\omega_{\rm SOT}\sin\theta_i,\end{aligned} \tag{A41}$$

$$\begin{aligned}f_i^\phi = &-\omega_{\rm ex}[\sin\theta_i\cos\theta_{3-i}-\sin\theta_{3-i}\cos\theta_i\cos(\phi_i\\ &-\phi_{3-i})]+(\omega_{\rm ea}+\omega_{\rm ha}\cos^2\phi_i)\sin 2\theta_i.\end{aligned} \tag{A42}$$

Including the small disturbance ($\delta\theta_i$ and $\delta\phi_i$) from equilibrium, we assume that $\theta_i = \theta_i^0+\delta\theta_i$ and $\phi_i = \phi_i^0+\delta\phi_i$. Inserting this ansatz into Eqs. (A39)–(A42), and keeping the linear terms of $\delta\theta_i$ and $\delta\phi_i$, the linearized equations are written as

$$\mathcal{C}\dot{\mathbf{y}} = \mathcal{D}\mathbf{y}, \tag{A43}$$

where $\mathbf{y} = (\delta\theta_1, \delta\phi_1, \delta\theta_2, \delta\phi_2)^T$, with T denoting the matrix transpose,

$$\mathcal{C} = \begin{pmatrix} 1 & \alpha & 0 & 0 \\ -\alpha & 1 & 0 & 0 \\ 0 & 0 & 1 & \alpha \\ 0 & 0 & -\alpha & 1 \end{pmatrix}, \tag{A44}$$

and $\mathcal{D}$ is the Jacobian matrix at the equilibrium,

$$\mathcal{D} = \begin{pmatrix} \frac{\partial f_1^\theta}{\partial\theta_1} & \frac{\partial f_1^\theta}{\partial\phi_1} & \frac{\partial f_1^\theta}{\partial\theta_2} & \frac{\partial f_1^\theta}{\partial\phi_2} \\ \frac{\partial f_1^\phi}{\partial\theta_1} & \frac{\partial f_1^\phi}{\partial\phi_1} & \frac{\partial f_1^\phi}{\partial\theta_2} & \frac{\partial f_1^\phi}{\partial\phi_2} \\ \frac{\partial f_2^\theta}{\partial\theta_1} & \frac{\partial f_2^\theta}{\partial\phi_1} & \frac{\partial f_2^\theta}{\partial\theta_2} & \frac{\partial f_2^\theta}{\partial\phi_2} \\ \frac{\partial f_2^\phi}{\partial\theta_1} & \frac{\partial f_2^\phi}{\partial\phi_1} & \frac{\partial f_2^\phi}{\partial\theta_2} & \frac{\partial f_2^\phi}{\partial\phi_2} \end{pmatrix}_{\theta_i=\theta_i^0,\phi_i=\phi_i^0}. \tag{A45}$$

Then taking the oscillating ansatz ($\delta\theta_i$, $\delta\phi_i \propto e^{\lambda t}$) into Eq. (A43), the existence of a nontrivial solution demands that λ satisfies the secular equation as Eq. (A31), where the parameters are listed as

$$a_0 = 1 + \alpha^2, \tag{A46}$$

$$a_1 = \alpha[2\omega_{\rm ex} - 2\omega_{\rm ea} - \omega_{\rm ha} + 3(-1)^P M], \tag{A47}$$

$$\begin{aligned} a_2 = &-2[\omega_{\rm ex} + (-1)^P M] \\ &\times [2\omega_{\rm ea} + \omega_{\rm ha} - (-1)^P M], \end{aligned} \tag{A48}$$

$$b_0 = 1 + \alpha^2, \tag{A49}$$

$$b_1 = \alpha[2\omega_{\rm ex} - 2\omega_{\rm ea} - \omega_{\rm ha} + 3(-1)^P M], \tag{A50}$$

$$b_2 = 2M[(-1)^P(2\omega_{\rm ex} - 2\omega_{\rm ea} - \omega_{\rm ha}) + M], \tag{A51}$$

where $M = \sqrt{\omega_{\rm ha}^2 - \omega_{\rm SOT}^2}$. It is easy to observe that $a_2 < 0$ for $P = 1, 2, 3, 4$. Thus, taking into account the Routh-Hurwitz criterion [78–80], these four tilted-AFM states are all unstable.

4. Stability analysis of tilted-FM states

The equilibria are $\theta_{1,2}^0 = \pi/2$ and $\phi_i^0 = \phi^0$, with ϕ^0 being Eq. (A4). Using the same method as in Appendix A 3, a secular equation such as Eq. (A31) is obtained with the parameters listed as

$$a_0 = 1 + \alpha^2, \tag{A52}$$

$$a_1 = -\alpha[2\omega_{\rm ea} + \omega_{\rm ha} - 3(-1)^P M], \tag{A53}$$

$$a_2 = 2M[M - (-1)^P(2\omega_{\rm ea} + \omega_{\rm ha})], \tag{A54}$$

$$b_0 = 1 + \alpha^2, \tag{A55}$$

$$b_1 = -\alpha[4\omega_{\rm ex} + 2\omega_{\rm ea} + \omega_{\rm ha} - 3(-1)^P M], \tag{A56}$$

$$\begin{aligned} b_2 = &\, 2[\omega_{\rm ex} - (-1)^P M] \\ &\times [2\omega_{\rm ex} + 2\omega_{\rm ea} + \omega_{\rm ha} - (-1)^P M]. \end{aligned} \tag{A57}$$

Apparently, if $\omega_{\rm ex} > \omega_{\rm ha}$, $b_1 < 0$ for $P = 1, 2, 3, 4$. So, according to the Routh-Hurwitz criterion [78–80], these four tilted-FM states are all unstable.

APPENDIX B: EQUILIBRIA AND THEIR STABILITIES FOR CASE II

In this case, the spin polarization is along the hard axis. So, we can take $\mathbf{u}_p = \mathbf{u}_{\rm ha} = \mathbf{e}_z$ and $\mathbf{u}_{\rm ea} = \mathbf{e}_y$. The balance between the SOT and the precessional torques produces the equilibrium equation, using spherical coordinates, which read,

$$\begin{aligned} &\left(\omega_{\rm SOT} - \omega_{\rm ea}\sin 2\phi_i^0\right)\sin\theta_i^0 \\ &\quad = \omega_{\rm ex}\sin\left(\phi_i^0 - \phi_{3-i}^0\right)\sin\theta_{3-i}^0, \end{aligned} \tag{B1}$$

$$\begin{aligned} &\left[\omega_{\rm ex}\cos\theta_{3-i}^0 + 2\left(\omega_{\rm ha} + \omega_{\rm ea}\sin^2\phi_i^0\right)\cos\theta_i^0\right]\sin\theta_i^0 \\ &\quad = \omega_{\rm ex}\cos\left(\phi_i^0 - \phi_{3-i}^0\right)\cos\theta_i^0\sin\theta_{3-i}^0. \end{aligned} \tag{B2}$$

Inspection of Eqs. (B1) and (B2) leads to a first kind of solutions that satisfy $\sin\theta_i^0 = 0$. This yields the $\mathbf{u}_p$-FM states ($\theta_i^0 = 0$ or π) with $\mathbf{m}_i^0$ in the direction of $\mathbf{u}_p$, and the $\mathbf{u}_p$-AFM states in which $\theta_1^0 = 0\ (\pi)$ and $\theta_2^0 = \pi\ (0)$.

For $\sin\theta_i^0 \neq 0$, Eqs. (B1) and (B2) allow $\sin 2\phi_i^0 = \omega_{\rm SOT}/\omega_{\rm ea}$, $\sin(\phi_1^0 - \phi_2^0) = 0$, and $\cos\theta_i^0 = 0$. These generate four tilted-FM states in which $\theta_i^0 = \pi/2$ and $\phi_i^0 = \phi^0$, and four tilted-AFM states in which $\theta_i = \pi/2$, $\phi_1^0 = \phi^0$, and $\phi_2^0 = \pi + \phi^0$. ϕ^0 reads,

$$\phi^0 = \frac{1}{2}\left[(P-1)\pi - (-1)^P \arcsin\frac{\omega_{\rm SOT}}{\omega_{\rm ea}}\right], \tag{B3}$$

with $P = 1, 2, 3, 4$. For these equilibria, $\mathbf{m}_i$ are located in the x-y plane and deviate from the easy axis. In the following, we will derive the stable regions of the above four kinds of equilibria by the linear stability analysis.

1. Stability analysis of $\mathbf{u}_p$-AFM states

For these states, $\mathbf{m}_1^0 = \eta\mathbf{e}_z$ and $\mathbf{m}_2^0 = -\eta\mathbf{e}_z$ with $\eta = \pm 1$. Following the same procedure as in Appendix A 1, and taking $\mathbf{u}_p = \mathbf{u}_{\rm ha} = \mathbf{e}_z$ and $\mathbf{u}_{\rm ea} = \mathbf{e}_y$ in the derivation, a secular equation such as Eq. (A12) is obtained with the parameters listed as

$$a_0 = (1 + \alpha^2)^2, \tag{B4}$$

$$a_1 = 4\alpha(1 + \alpha^2)(\omega_{\rm ex} - \omega_{\rm ea} - 2\omega_{\rm ha}), \tag{B5}$$

$$\begin{aligned} a_2 = 2\big\{&4\omega_{\rm ha}(\omega_{\rm ea} + \omega_{\rm ha}) - 2(\omega_{\rm ea} + 2\omega_{\rm ha})\omega_{\rm ex} \\ &+ 2\alpha^2\big[\omega_{\rm ex}^2 - 3(\omega_{\rm ea} + 2\omega_{\rm ha})\omega_{\rm ex} \\ &+ \omega_{\rm ea}^2 + 6\omega_{\rm ea}\omega_{\rm ha} + 6\omega_{\rm ha}^2\big] - (1 - \alpha^2)\omega_{\rm SOT}^2\big\}, \end{aligned} \tag{B6}$$

$$\begin{aligned} a_3 = &\, 4\alpha(\omega_{\rm ex} - \omega_{\rm ea} - 2\omega_{\rm ha})[4\omega_{\rm ha}(\omega_{\rm ea} + \omega_{\rm ha}) \\ &- 2(\omega_{\rm ea} + 2\omega_{\rm ha})\omega_{\rm ex} + \omega_{\rm SOT}^2], \end{aligned} \tag{B7}$$

$$\begin{aligned} a_4 = &\left[4\omega_{\rm ha}(\omega_{\rm ea} + \omega_{\rm ha}) + \omega_{\rm SOT}^2\right] \\ &\times \left[4(\omega_{\rm ex} - \omega_{\rm ha})(\omega_{\rm ex} - \omega_{\rm ea} - \omega_{\rm ha}) + \omega_{\rm SOT}^2\right]. \end{aligned} \tag{B8}$$

By use of Eqs. (A18)–(A21), the Routh-Hurwitz determinants are derived,

$$\Delta_1 = 4\alpha(1+\alpha^2)(\omega_{\rm ex}-\omega_{\rm ea}-2\omega_{\rm ha}), \tag{B9}$$

$$\Delta_2 = \Delta_1\big[-2(f1-\alpha^2 f2)-(3-\alpha^2)\omega_{\rm SOT}^2\big], \tag{B10}$$

$$\Delta_3 = \frac{4\Delta_1^2}{1+\alpha^2}\big[\omega_{\rm ea}^2\omega_{\rm ex}^2-\alpha^2 f3f4 - (f3+\alpha^2 f4)\omega_{\rm SOT}^2-\omega_{\rm SOT}^4\big], \tag{B11}$$

$$\Delta_4 = a_4\Delta_3, \tag{B12}$$

where

$$f_1 = (\omega_{\rm ea}+2\omega_{\rm ha})\omega_{\rm ex}-2\omega_{\rm ha}(\omega_{\rm ea}+\omega_{\rm ha}), \tag{B13}$$

$$f_2 = 2\omega_{\rm ex}^2-5(\omega_{\rm ea}+2\omega_{\rm ha})\omega_{\rm ex} + 2\big(\omega_{\rm ea}^2+5\omega_{\rm ea}\omega_{\rm ha}+5\omega_{\rm ha}^2\big), \tag{B14}$$

$$f_3 = (\omega_{\rm ex}-2\omega_{\rm ha})(\omega_{\rm ex}-2\omega_{\rm ea}-2\omega_{\rm ha}), \tag{B15}$$

$$f_4 = (\omega_{\rm ea}+2\omega_{\rm ha})(2\omega_{\rm ex}-\omega_{\rm ea}-2\omega_{\rm ha}). \tag{B16}$$

If $\Delta_1 > 0$, we have $\omega_{\rm ex} > \omega_{\rm ea}+2\omega_{\rm ha}$. This results in $a_4 > 0$, $f_1 > 0$, and $f_4 > 0$. By now, the stability requires positive Δ_2 and Δ_3. Considering $\alpha^2 < 3$, the necessary condition for $\Delta_2 > 0$ is $f_1-\alpha^2 f_2 < 0$. If $f_2 < 0$, this inequality is unsatisfied and $\Delta_2 < 0$. If $f_2 > 0$, we obtain the necessary condition $\alpha^2 > f_1/f_2$ for $\Delta_2 > 0$. Additionally, if $f_3 > 0$, the necessary condition for $\Delta_3 > 0$ is $\alpha^2 < \omega_{\rm ea}^2\omega_{\rm ex}^2/(f3f4)$. So, to ensure $\Delta_2 > 0$ and $\Delta_3 > 0$ simultaneously, the damping constant must satisfy $f_1/f_2 < \alpha^2 < \omega_{\rm ea}^2\omega_{\rm ex}^2/(f3f4)$. Unfortunately, it can be proved that $f_1/f_2 > \omega_{\rm ea}^2\omega_{\rm ex}^2/(f3f4)$ for $\omega_{\rm ex} > \omega_{\rm ea} + 2\omega_{\rm ha}$. Δ_2 and Δ_3 cannot be positive simultaneously for $f_3 > 0$. If $f_3 < 0$, we have $\omega_{\rm ea}+2\omega_{\rm ha} < \omega_{\rm ex} < 2\omega_{\rm ea}+2\omega_{\rm ha}$. In this range, it is easy to infer that $f_2 < 0$ and $\Delta_2 < 0$. In summary, whether f_2 and f_3 are positive or negative, Δ_2 and Δ_3 cannot be positive simultaneously. Finally, it can be concluded that the $\mathbf{u}_p$-AFM states are unstable.

2. Stability analysis of $\mathbf{u}_p$-FM states

For these states, $\mathbf{m}_i^0 = \eta\mathbf{e}_z$ with $\eta = \pm1$. After taking $\mathbf{u}_p = \mathbf{u}_{\rm ha} = \mathbf{e}_z$ and $\mathbf{u}_{\rm ea} = \mathbf{e}_y$ in the derivation, like Appendix A 2, the secular equation is factorized into the product of two second-order polynomials such as Eq. (A31) with the parameters

$$a_0 = 1+\alpha^2, \tag{B17}$$

$$a_1 = 2[-\alpha(\omega_{\rm ea}+2\omega_{\rm ha})+\eta\omega_{\rm SOT}], \tag{B18}$$

$$a_2 = 4\omega_{\rm ha}(\omega_{\rm ea}+\omega_{\rm ha})+\omega_{\rm SOT}^2, \tag{B19}$$

$$b_0 = 1+\alpha^2, \tag{B20}$$

$$b_1 = 2[-\alpha(2\omega_{\rm ex}+\omega_{\rm ea}+2\omega_{\rm ha})+\eta\omega_{\rm SOT}], \tag{B21}$$

$$b_2 = 4(\omega_{\rm ex}+\omega_{\rm ha})(\omega_{\rm ex}+\omega_{\rm ea}+\omega_{\rm ha})+\omega_{\rm SOT}^2. \tag{B22}$$

If $\eta\omega_{\rm SOT} > \alpha(2\omega_{\rm ex}+\omega_{\rm ea}+2\omega_{\rm ha})]$, a_1, a_2, b_1, and b_2 are all positive. Thus, in view of the Routh-Hurwitz criterion [78–80], the $\mathbf{u}_p$-FM state with $\mathbf{m}_i^0 = \mathbf{e}_z$ is stable if $\omega_{\rm SOT} > \omega_{\rm SOT}^u$, while $\omega_{\rm SOT} < -\omega_{\rm SOT}^u$ is the stable condition of the FM state with $\mathbf{m}_i^0 = -\mathbf{e}_z$. The critical value is

$$\omega_{\rm SOT}^u = \alpha(2\omega_{\rm ex}+\omega_{\rm ea}+2\omega_{\rm ha}). \tag{B23}$$

3. Stability analysis of tilted-AFM states

For these states, $\theta_{1,2}^0 = \pi/2$, $\phi_1^0 = \phi^0$, and $\phi_2^0 = \pi+\phi^0$, with ϕ^0 being Eq. (B3). By the method used in Appendix A 3, and taking $\mathbf{u}_p = \mathbf{u}_{\rm ha} = \mathbf{e}_z$ and $\mathbf{u}_{\rm ea} = \mathbf{e}_y$ in the derivation, a secular equation such as Eq. (A31) is obtained with the parameters listed as

$$a_0 = 1+\alpha^2, \tag{B24}$$

$$a_1 = \alpha[2\omega_{\rm ex}+\omega_{\rm ea}+2\omega_{\rm ha}+3(-1)^P N], \tag{B25}$$

$$a_2 = 2N[(-1)^P(2\omega_{\rm ex}+\omega_{\rm ea}+2\omega_{\rm ha})+N], \tag{B26}$$

$$b_0 = 1+\alpha^2, \tag{B27}$$

$$b_1 = \alpha[2\omega_{\rm ex}+\omega_{\rm ea}+2\omega_{\rm ha}+3(-1)^P N], \tag{B28}$$

$$b_2 = 2[\omega_{\rm ex}+(-1)^P N][\omega_{\rm ea}+2\omega_{\rm ha}+(-1)^P N], \tag{B29}$$

where $N = \sqrt{\omega_{\rm ea}^2-\omega_{\rm SOT}^2}$. Evidently, a_1, a_2, b_1, and b_2 are all positive for $P = 2, 4$. According to the Routh-Hurwitz criterion [78–80], these two equivalent tilted-AFM states are stable, which is expressed as $\theta_{1,2}^0 = \pi/2$, $\phi_1^0 = 1/2[\pi - \arcsin(\omega_{\rm SOT}/\omega_{\rm ea})]$, and $\phi_2^0 = \pi+\phi_1^0$.

4. Stability analysis of tilted-FM states

For these states, $\theta_{1,2}^0 = \pi/2$, $\phi_{1,2}^0 = \phi^0$, with ϕ^0 being Eq. (B3). By the method used in Appendix A 3, and taking $\mathbf{u}_p = \mathbf{u}_{\rm ha} = \mathbf{e}_z$ and $\mathbf{u}_{\rm ea} = \mathbf{e}_y$ in the derivation, a secular equation such as Eq. (A31) is obtained with the parameters listed as

$$a_0 = 1+\alpha^2, \tag{B30}$$

$$a_1 = \alpha[\omega_{\rm ea}+2\omega_{\rm ha}+3(-1)^P N], \tag{B31}$$

$$a_2 = 2N[(-1)^P(\omega_{\rm ea}+2\omega_{\rm ha})+N], \tag{B32}$$

$$b_0 = 1+\alpha^2, \tag{B33}$$

$$b_1 = -\alpha[4\omega_{\rm ex}-\omega_{\rm ea}-2\omega_{\rm ha}-3(-1)^P N], \tag{B34}$$

$$b_2 = 2[\omega_{\rm ex}-(-1)^P N] \times [2\omega_{\rm ex}-\omega_{\rm ea}-2\omega_{\rm ha}-(-1)^P N]. \tag{B35}$$

Obviously, $a_2 < 0$ for $P = 1, 3$. For $P = 2, 4$, from $b_1 > 0$, we have $4\omega_{\rm ex} < \omega_{\rm ea}+2\omega_{\rm ha}+3\sqrt{\omega_{\rm ea}^2-\omega_{\rm SOT}^2}$, while from $b_2 > 0$, $4\omega_{\rm ex} > 2\omega_{\rm ea}+4\omega_{\rm ha}+2\sqrt{\omega_{\rm ea}^2-\omega_{\rm SOT}^2}$. These two inequalities are conflicting. Thus, a_1, a_2, b_1, and b_2 cannot be positive simultaneously. Taking into account the Routh-Hurwitz criterion [78–80], these four tilted-FM states are all unstable.

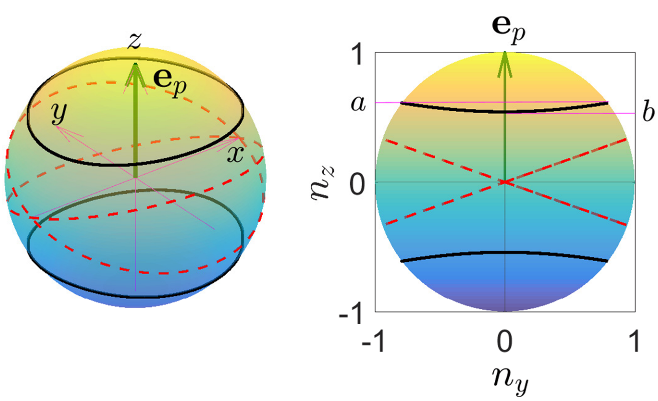

FIG. 9. Schematic view of the constant-energy orbits (black solid curves) around the spin polarization $\mathbf{u}_p$. The red dashed curves are through the saddle points of Eq. (10). The right panel is the projection of the orbits on the y-z plane. We should emphasize that the orbits are made to be seen clearly, and the corresponding values of adopted parameters are not used to analyze self-oscillations in the main text.

APPENDIX C: DERIVATIONS OF EQS. (15) and (17)

In this Appendix, for Case I, we use the averaging technique [47,48] to derive the strength of SOT [Eq. (15)] to excite a self-oscillation and the corresponding frequency [Eq. (17)].

To perform the integrals of Eqs. (13) and (14), it is essential to define the constant-energy orbits, which are the intersection of the hyperbolic cylindrical surfaces [Eq. (10)] and the unit sphere ($|\mathbf{n}| = 1$), as shown by the black solid curves as examples in the left panel of Fig. 9. These orbits are identified by the energy $\mathcal{E}_n$. For certain $\mathcal{E}_n$, there are two branches on both sides of the equator. When $\mathcal{E}_n = \omega_{\rm ex} - \omega_{\rm ea}$, these orbits shrink to points in the north or south poles. When $\mathcal{E}_n = \omega_{\rm ha}$, these orbits degenerate to those through the saddle points of Eq. (10), as shown by the red dashed curves in Fig. 9.

The exchange torques drive $\mathbf{m}_1$ and $\mathbf{m}_2$ to rotate left-handedly. So, the damping torques drive $\mathbf{m}_1$ and $\mathbf{m}_2$ far away from the z axis. For the upper (lower) orbit, only the SOT with $\omega_{\rm SOT} > 0\,(<0)$ can counteract the damping torque and sustain a stable oscillation.

Projecting on the y-z plane, the orbits are parts of the hyperbolic curves, as shown in the right panel of Fig. 9. From Eq. (10), the curves are defined by $n_z^2/a_z^2 - n_y^2/a_y^2 = 1$ with $a_z = \sqrt{\mathcal{E}_n - \omega_{\rm ha}}/\sqrt{\omega_{\rm ex} - \omega_{\rm ea} - \omega_{\rm ha}}$, and $a_y = \sqrt{\mathcal{E}_n - \omega_{\rm ha}}/\sqrt{\omega_{\rm ha}}$. Observing the curves on the sphere surface, when $n_x = 0$, n_z is maximum. When $n_y = 0$, n_z is minimum. Then, the maximal and minimal values of n_z are obtained as

$$a = \sqrt{\frac{\mathcal{E}_n}{\omega_{\rm ex} - \omega_{\rm ea}}}, \tag{C1}$$

$$b = \sqrt{\frac{\mathcal{E}_n - \omega_{\rm ha}}{\omega_{\rm ex} - \omega_{\rm ea} - \omega_{\rm ha}}}. \tag{C2}$$

By use of Eq. (10) and the unit constraint of $\mathbf{n}$, we express n_x and n_y by n_z and replace dt by $dn_z/(dn_z/dt)$ with dn_z/dt obtained by Eq. (9). Then, considering the reflection symmetries along the x and y axes, the loop integrals of Eqs. (13) and (14) can be divided into four equivalent parts. Finally, keeping the first-order terms of α and $\omega_{\rm SOT}$, Eqs. (13) and (14) are written as

$$\mathcal{W}_{\rm damp} = 8\alpha\left[\sqrt{\omega_{\rm ex} - \omega_{\rm ea}}\sqrt{\omega_{\rm ex} - \omega_{\rm ea} - \omega_{\rm ha}}I_2 - \frac{\mathcal{E}_n(\mathcal{E}_n - \omega_{\rm ha})}{\sqrt{\omega_{\rm ex} - \omega_{\rm ea}}\sqrt{\omega_{\rm ex} - \omega_{\rm ea} - \omega_{\rm ha}}}I_0\right], \tag{C3}$$

$$\mathcal{W}_{\rm SOT} = 4\omega_{\rm SOT}\frac{\omega_{\rm ex} - \omega_{\rm ea} - \mathcal{E}_n}{\sqrt{\omega_{\rm ex} - \omega_{\rm ea}}\sqrt{\omega_{\rm ex} - \omega_{\rm ea} - \omega_{\rm ha}}}I_1, \tag{C4}$$

where

$$I_p = \int_b^a \frac{(n_z)^p dn_z}{\sqrt{a^2 - n_z^2}\sqrt{n_z^2 - b^2}}, \tag{C5}$$

with $p = 0, 1, 2$. Taking a substitution $n_z = \sqrt{a^2 - (a^2 - b^2)s^2}$, Eq. (C5) becomes

$$I_p = a^{p-1}\int_0^1 ds\frac{(\sqrt{1 - k^2s^2})^p}{\sqrt{1 - s^2}\sqrt{1 - k^2s^2}}, \tag{C6}$$

with the modulus

$$k = \sqrt{1 - \frac{b^2}{a^2}} = \sqrt{\frac{\omega_{\rm ha}(\omega_{\rm ex} - \omega_{\rm ea} - \mathcal{E}_n)}{\mathcal{E}_n(\omega_{\rm ex} - \omega_{\rm ea} - \omega_{\rm ha})}}. \tag{C7}$$

Specifically, the three integrals are calculated as

$$I_0 = \frac{1}{a}\int_0^1 \frac{ds}{\sqrt{1 - s^2}\sqrt{1 - k^2s^2}} = \sqrt{\frac{\omega_{\rm ex} - \omega_{\rm ea}}{\mathcal{E}_n}}\mathsf{K}(k), \tag{C8}$$

$$I_1 = \int_0^1 \frac{ds}{\sqrt{1 - s^2}} = \frac{\pi}{2}, \tag{C9}$$

$$I_2 = a\int_0^1 ds\frac{\sqrt{1 - k^2s^2}}{\sqrt{1 - s^2}} = \sqrt{\frac{\mathcal{E}_n}{\omega_{\rm ex} - \omega_{\rm ea}}}\mathsf{E}(k), \tag{C10}$$

where $\mathsf{E}(k)$ and $\mathsf{K}(k)$ are the complete elliptic integrals of the second and first kinds. Substituting Eqs. (C8)–(C10) into Eqs. (C3) and (C4) yields Eq. (15) from Eq. (12).

By a similar procedure, the precessional period is derived as

$$T = 4\int_b^a \frac{dn_z}{dn_z/dt} = \frac{2I_0}{\sqrt{\omega_{\rm ex} - \omega_{\rm ea}}\sqrt{\omega_{\rm ex} - \omega_{\rm ea} - \omega_{\rm ha}}}. \tag{C11}$$

Inserting Eq. (C8) into Eq. (C11), Eq. (17) is obtained via $f = 1/T$.

APPENDIX D: DERIVATIONS OF EQS. (24) and (26)

Here, for Case II, we derive the strength of SOT [Eq. (24)] to excite a self-oscillation and the corresponding frequency [Eq. (26)], with the same procedure as Appendix C, just taking different reduced energy, which is Eq. (23). From it, the maximal and minimal values of n_z are obtained as

$$a = \sqrt{\frac{\mathcal{E}_n + \omega_{\rm ea}}{\omega_{\rm ex} + \omega_{\rm ea} + \omega_{\rm ha}}}, \tag{D1}$$

$$b = \sqrt{\frac{\mathcal{E}_n}{\omega_{\rm ex} + \omega_{\rm ha}}}, \tag{D2}$$

and the integrals of Eqs. (13) and (14) are expressed as

$$\mathcal{W}_{\text{damp}} = 8\alpha\left[\sqrt{\omega_{\text{ex}}+\omega_{\text{ha}}}\sqrt{\omega_{\text{ex}}+\omega_{\text{ea}}+\omega_{\text{ha}}}I_2 - \frac{\mathcal{E}_n(\mathcal{E}_n+\omega_{\text{ea}})}{\sqrt{\omega_{\text{ex}}+\omega_{\text{ha}}}\sqrt{\omega_{\text{ex}}+\omega_{\text{ea}}+\omega_{\text{ha}}}}I_0\right], \quad \text{(D3)}$$

$$\mathcal{W}_{\text{SOT}} = 4\omega_{\text{SOT}}\frac{\omega_{\text{ex}}+\omega_{\text{ha}}-\mathcal{E}_n}{\sqrt{\omega_{\text{ex}}+\omega_{\text{ha}}}\sqrt{\omega_{\text{ex}}+\omega_{\text{ea}}+\omega_{\text{ha}}}}I_1, \quad \text{(D4)}$$

where

$$I_p = \int_b^a \frac{(n_z)^p dn_z}{\sqrt{a^2-n_z^2}\sqrt{n_z^2-b^2}}, \quad \text{(D5)}$$

with $p = 0, 1, 2$. Taking a substitution $n_z = \sqrt{a^2-(a^2-b^2)s^2}$, Eq. (D5) becomes

$$I_p = a^{p-1}\int_0^1 ds\frac{(\sqrt{1-k^2s^2})^p}{\sqrt{1-s^2}\sqrt{1-k^2s^2}}, \quad \text{(D6)}$$

with the modulus

$$k = \sqrt{1-\frac{b^2}{a^2}} = \sqrt{\frac{\omega_{\text{ea}}(\omega_{\text{ex}}+\omega_{\text{ha}}-\mathcal{E}_n)}{(\omega_{\text{ea}}+\mathcal{E}_n)(\omega_{\text{ha}}+\mathcal{E}_n)}}. \quad \text{(D7)}$$

Specifically, the three integrals are calculated as

$$I_0 = \frac{1}{a}\int_0^1 \frac{ds}{\sqrt{1-s^2}\sqrt{1-k^2s^2}} = \sqrt{\frac{\omega_{\text{ex}}+\omega_{\text{ea}}+\omega_{\text{ha}}}{\mathcal{E}_n+\omega_{\text{ea}}}}\mathsf{K}(k), \quad \text{(D8)}$$

$$I_1 = \int_0^1 \frac{ds}{\sqrt{1-s^2}} = \frac{\pi}{2}, \quad \text{(D9)}$$

$$I_2 = a\int_0^1 ds\frac{\sqrt{1-k^2s^2}}{\sqrt{1-s^2}} = \sqrt{\frac{\mathcal{E}_n+\omega_{\text{ea}}}{\omega_{\text{ex}}+\omega_{\text{ea}}+\omega_{\text{ha}}}}\mathsf{E}(k). \quad \text{(D10)}$$

Substituting Eqs. (D8)–(D10) into Eqs. (D3) and (D4) allows us to get Eq. (24) from Eq. (12).

Additionally, the precessional period is derived as

$$T = 4\int_b^a \frac{dn_z}{dn_z/dt} = \frac{2I_0}{\sqrt{\omega_{\text{ex}}+\omega_{\text{ha}}}\sqrt{\omega_{\text{ex}}+\omega_{\text{ea}}+\omega_{\text{ha}}}}. \quad \text{(D11)}$$

Inserting Eq. (D8) into Eq. (D11), Eq. (26) is obtained via $f = 1/T$.

APPENDIX E: DERIVATIONS OF EQ. (21)

Unlike Case I, the lower threshold of the self-oscillation cannot be determined by the linear instability of the tilted-AFM state for case II. To make sense of the tilted-AFM state physically, Eq. (B3) implies that $\omega_{\text{SOT}} < \omega_{\text{SOT}}^c = \omega_{\text{ea}}$. In Fig. 10, we take $\omega_{\text{ea}} = 0.01\omega_{\text{ex}}$. A self-oscillation emerges when increasing ω_{SOT}^l to $0.0079\omega_{\text{ex}}$, which is smaller than ω_{SOT}^c ($0.01\omega_{\text{ex}}$). So, this ω_{SOT}^c is not the lower threshold of the self-oscillation.

To derive the lower threshold analytically, we utilize an averaging technique [16], which is in good agreement with the numeric result for the FM self-oscillation. Before doing that, we need to define two fixed points for the considered nonlinear magnetic system without the SOT. From Eq. (23), it is easy to infer that $n_y = 1$ ($m_{1y} = -m_{2y} = 1$) is a focus, as marked by the black dots in Figs. 10(a) and 10(b). Correspondingly, the energy $\mathcal{E}_{\min} = -\omega_{\text{ea}}$. Also, $n_x = 1$ ($m_{1x} = -m_{2x} = 1$) is a saddle, as marked by the blue circles, whose energy is $\mathcal{E}_{\text{saddle}} = 0$.

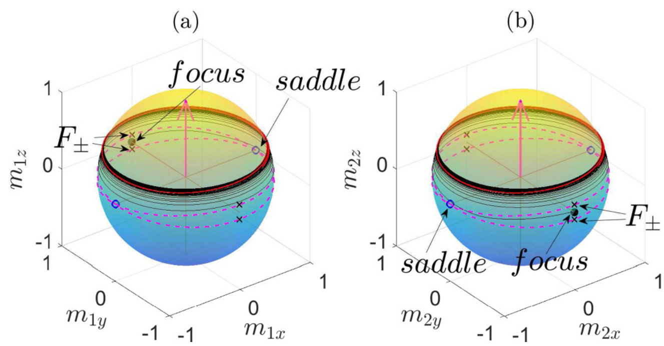

FIG. 10. Evolutions of $\mathbf{m}_1$ (a) and $\mathbf{m}_2$ (b) at the lower threshold ($\omega_{\text{SOT}}^l = 0.0079\omega_{\text{ex}}$) of the self-oscillation for Case II. The arrow denotes the spin-polarization direction. The black dots represent the initial states without the SOT. The red curves are the final orbits of evolutions. The dashed curves are the constant-energy orbits passing through the saddle points ($\mathcal{E}_n = 0$). Here, to identify clearly the curves, the parameters are taken as $\alpha = 0.01$, $\omega_{\text{ea}} = 0.01\omega_{\text{ex}}$, and $\omega_{\text{ha}} = 0.1\omega_{\text{ex}}$. Putting them into Eq. (21), the lower threshold $\omega_{\text{SOT}}^l = 0.0077\omega_{\text{ex}}$, which agrees well with the numerical calculations except for a slight difference.

Then, we maintain our attention on the evolutions of $\mathbf{m}_{1,2}$ at the lower threshold, as plotted in Figs. 10(a) and 10(b). In the absence of the SOT, $\mathbf{m}_1$ ($\mathbf{m}_2$) prefers to line up along the y ($-y$) direction initially, i.e., they are located at its focus. Applying a SOT at the lower threshold, $\mathbf{m}_{1,2}$ evolve from the foci to the saddle points, then enter their own constant-energy orbit. The trajectory between the focus and the saddle is not a constant-energy one. Therefore, before precessing in a constant-energy orbit, $\mathbf{m}_{1,2}$ ($\mathbf{n}$) should overcome an energy barrier $\mathcal{E}_{\text{saddle}} - \mathcal{E}_{\min} = \omega_{\text{ea}}$. In this startup stage, besides offsetting the damping, the SOT should do extra work to cross this barrier. On average, this work-energy relation reads

$$\omega_{\text{SOT}}\int_{\text{focus}}^{\text{saddle}} (\mathbf{n}\times\mathbf{e}_z)\cdot\left(\mathbf{n}\times\frac{d\mathcal{E}_n}{d\mathbf{n}}\right)dt = \alpha\int_{\text{focus}}^{\text{saddle}}\left(\mathbf{n}\times\frac{d\mathcal{E}_n}{d\mathbf{n}}\right)^2 dt + \omega_{\text{ea}}. \quad \text{(E1)}$$

The absence of an explicit expression for this part of the trajectory makes an exact analytical solution of Eq. (E1) untractable. Fortunately, in view of the strong exchange, $\omega_{\text{ex}} \gg \omega_{\text{ea}}$ generally. The constant-energy orbit through the saddle is very close to the x-y plane, as indicated in Figs. 10(a) and 10(b). By setting $\mathcal{E}_n = \mathcal{E}_{\text{saddle}} = 0$ in Eq. (23), we obtain the intersection points ($F_\pm$) between this orbit and the y-z plane, which are $(0, \pm\tilde{n}_y, \pm\tilde{n}_z)$, with $\tilde{n}_y = \sqrt{\omega_{\text{ex}}+\omega_{\text{ha}}}/\sqrt{\omega_{\text{ex}}+\omega_{\text{ea}}+\omega_{\text{ha}}}$ and $\tilde{n}_z = \sqrt{\omega_{\text{ea}}}/\sqrt{\omega_{\text{ex}}+\omega_{\text{ea}}+\omega_{\text{ha}}}$). Obviously, in view of $\omega_{\text{ea}} \ll \omega_{\text{ex}}$, $\tilde{n}_z \ll 1$. So, $F_\pm$ are very close to the focus, and the integral can be approximately completed along the constant-energy trajectory from F_+ or F_- to the saddle point.

Adopting this approximation, taking m_z as the integral variable, and utilizing Eq. (23), Eq. (E1) becomes

$$\omega_{\rm SOT}\sqrt{\omega_{\rm ex}+\omega_{\rm ha}}\sqrt{\omega_{\rm ex}+\omega_{\rm ea}+\omega_{\rm ha}}\int_{\tilde{n}_z}^{0}\frac{2m_z dm_z}{\sqrt{\tilde{n}_z^2-m_z^2}}$$

$$=\alpha\frac{\sqrt{\omega_{\rm ex}+\omega_{\rm ha}}}{\sqrt{\omega_{\rm ex}+\omega_{\rm ea}+\omega_{\rm ha}}}\int_{\tilde{n}_z}^{0}\frac{dm_z}{\sqrt{\tilde{n}_z^2-m_z^2}}+\omega_{\rm ea}. \quad \text{(E2)}$$

Performing integration and solving Eq. (E2) for $\omega_{\rm SOT}$ yields the lower threshold, i.e., Eq. (21).

The analytic lower threshold Eq. (21) agrees very well with the numeric result. This is because the constant-energy orbit through the saddle points is very close to the x-y plane, i.e., $\omega_{\rm ea} \ll \omega_{\rm ex}$. Fortunately, Fig. 6 shows that the self-oscillation exists for small $\omega_{\rm ea}$, especially when $\alpha \lesssim 0.01$. Therefore, the approximation is self-consistent in performing the integrals of Eq. (E1).

[1] A. Jenkins, Phys. Rep. **525**, 167 (2013).
[2] D. C. Ralph and M. D. Stiles, J. Magn. Magn. Mater. **320**, 1190 (2008).
[3] A. Manchon, J. Železný, I. M. Miron, T. Jungwirth, J. Sinova, A. Thiaville, K. Garello, and P. Gambardella, Rev. Mod. Phys. **91**, 035004 (2019).
[4] J. Sun, Nature **425**, 359 (2003).
[5] S. I. Kiselev, J. C. Sankey, I. N. Krivorotov, N. C. Emley, R. J. Schoelkopf, R. A. Buhrman, and D. C. Ralph, Nature (London) **425**, 380 (2003).
[6] J. Xiao, A. Zangwill, and M. D. Stiles, Phys. Rev. B **72**, 014446 (2005).
[7] G. Bertotti, C. Serpico, I. D. Mayergoyz, A. Magni, M. d'Aquino, and R. Bonin, Phys. Rev. Lett. **94**, 127206 (2005).
[8] U. Ebels, D. Houssameddine, I. Firastrau, D. Gusakova, C. Thirion, B. Dieny, and L. D. Buda-Prejbeanu, Phys. Rev. B **78**, 024436 (2008).
[9] T. Taniguchi, H. Arai, S. Tsunegi, S. Tamaru, H. Kubota, and H. Imamura, Appl. Phys. Expr. **6**, 123003 (2013).
[10] T. Taniguchi, H. Arai, H. Kubota, and H. Imamura, IEEE Trans. Magn. **50**, 1400404 (2014).
[11] T. Taniguchi, S. Tsunegi, H. Kubota, and H. Imamura, Appl. Phys. Lett. **104**, 152411 (2014).
[12] D. Pinna, D. L. Stein, and A. D. Kent, Phys. Rev. B **90**, 174405 (2014).
[13] T. Taniguchi, S. Tsunegi, H. Kubota, and H. Imamura, J. Appl. Phys. **117**, 17C504 (2015).
[14] T. Taniguchi, T. Ito, Y. Utsumi, S. Tsunegi, and H. Kubota, J. Appl. Phys. **118**, 053903 (2015).
[15] T. Taniguchi, Phys. Rev. B **91**, 104406 (2015).
[16] T. Taniguchi and H. Kubota, Phys. Rev. B **93**, 174401 (2016).
[17] T. Taniguchi, T. Ito, S. Tsunegi, H. Kubota, and Y. Utsumi, Phys. Rev. B **96**, 024406 (2017).
[18] I. Firastrau, L. D. Buda-Prejbeanu, B. Dieny, and U. Ebels, J. Appl. Phys. **113**, 113908 (2013).
[19] Y. Zhou, J. Xiao, G. E. W. Bauer, and F. C. Zhang, Phys. Rev. B **87**, 020409(R) (2013).
[20] Ø. Johansen and J. Linder, Sci. Rep. **6**, 33845 (2016).
[21] H. Zhong, S. Qiao, S. Yan, L. Liang, Y. Zhao, and S. Kang, J. Magn. Magn. Mater. **497**, 166070 (2020).
[22] Q. Zhang, Y. Yang, Z. Luo, Y. Xu, R. Nie, X. Zhang, and Y. Wu, Phys. Rev. Appl. **13**, 054016 (2020).
[23] R. Cheng, M. W. Daniels, J.-G. Zhu, and D. Xiao, Phys. Rev. B **91**, 064423 (2015).
[24] R. Cheng, D. Xiao, and A. Brataas, Phys. Rev. Lett. **116**, 207603 (2016).
[25] R. Khymyn, I. Lisenkov, V. Tiberkevich, B. A. Ivanov, and A. Slavin, Sci. Rep. **7**, 43705 (2017).
[26] R. Zarzuela and Y. Tserkovnyak, Phys. Rev. B **95**, 180402(R) (2017).
[27] O. R. Sulymenko, O. V. Prokopenko, V. S. Tiberkevich, A. N. Slavin, B. A. Ivanov, and R. S. Khymyn, Phys. Rev. Appl. **8**, 064007 (2017).
[28] J. Chciński, M. Frankowski, and T. Stobiecki, Phys. Rev. B **96**, 174438 (2017).
[29] X. Z. Chen, R. Zarzuela, J. Zhang, C. Song, X. F. Zhou, G. Y. Shi, F. Li, H. A. Zhou, W. J. Jiang, F. Pan, and Y. Tserkovnyak, Phys. Rev. Lett. **120**, 207204 (2018).
[30] P. Stremoukhov, A. Safin, M. Logunov, S. Nikitov, and A. Kirilyuk, J. Appl. Phys. **125**, 223903 (2019).
[31] V. Puliafito, R. Khymyn, M. Carpentieri, B. Azzerboni, V. Tiberkevich, A. Slavin, and G. Finocchio, Phys. Rev. B **99**, 024405 (2019).
[32] R. E. Troncoso, K. Rode, P. Stamenov, J. M. D. Coey, and A. Brataas, Phys. Rev. B **99**, 054433 (2019).
[33] D.-K. Lee, B.-G. Park, and K.-J. Lee, Phys. Rev. Appl. **11**, 054048 (2019).
[34] A. Parthasarathy, E. Cogulu, A. D. Kent, and S. Rakheja, Phys. Rev. B **103**, 024450 (2021).
[35] G. Consolo, G. Valenti, A. R. Safin, S. A. Nikitov, V. Tyberkevich, and A. Slavin, Phys. Rev. B **103**, 134431 (2021).
[36] B. Wolba, O. Gomonay, and V. P. Kravchuk, Phys. Rev. B **104**, 024407 (2021).
[37] Q.-H. Li, P.-B. He, M.-Q. Cai, and Z.-D. Li, New J. Phys. **23**, 113020 (2021).
[38] O. V. Gomonay and V. M. Loktev, Low Temp. Phys. **41**, 698 (2015).
[39] G. Gurung, D.-F. Shao, and E. Y. Tsymbal, Phys. Rev. B **101**, 140405(R) (2020).
[40] Y. Takeuchi, Y. Yamane, J.-Y. Yoon, R. Itoh, B. Jinnai, S. Kanai, J. Ieda, S. Fukami, and H. Ohno, Nat. Mater. **20**, 1364 (2021).
[41] D.-Y. Zhao, P.-B. He, and M.-Q. Cai, Phys. Rev. B **104**, 214423 (2021).
[42] A. Shukla and S. Rakheja, Phys. Rev. Appl. **17**, 034037 (2022).
[43] I. Lisenkov, R. Khymyn, J. Åkerman, N. X. Sun, and B. A. Ivanov, Phys. Rev. B **100**, 100409(R) (2019).
[44] F. Cutugno, L. Sanchez-Tejerina, R. Tomasello, M. Carpentieri, and G. Finocchio, Appl. Phys. Lett. **118**, 052403 (2021).
[45] M. Guo, H. Zhang, and R. Cheng, Phys. Rev. B **105**, 064410 (2022).
[46] V. Baltz, A. Manchon, M. Tsoi, T. Moriyama, T. Ono, and Y. Tserkovnyak, Rev. Mod. Phys. **90**, 015005 (2018).

[47] G. Bertotti, I. D. Mayergoyz, and C. Serpico, *Nonlinear Magnetization Dynamics in Nanosystems* (Elsevier, Amsterdam, 2009), pp. 100–105 and 242–260.
[48] A. Thiaville and Y. Nakatani, *Spin Dynamics in Confined Magnetic Structures III*, edited by B. Hillebrands and A. Thiaville (Springer, New York, 2006), pp. 269–274 and 295–300.
[49] L. Zhu, D. C. Ralph, and R. A. Buhrman, Phys. Rev. Appl. **10**, 031001(R) (2018).
[50] C.-F. Pai, Y. Ou, L. H. Vilela-Leão, D. C. Ralph, and R. A. Buhrman, Phys. Rev. B **92**, 064426 (2015).
[51] Z. L. Wang, H. Y. Cheng, K. W. Shi, Y. Liu, J. F. Qiao, D. Q. Zhu, W. L. Cai, X. Y. Zhang, S. Eimer, D. P. Zhu, J. Zhang, A. Fert, and W. S. Zhao, Nanoscale **12**, 15246 (2020).
[52] M. T. Hutchings and E. J. Samuelsen, Phys. Rev. B **6**, 3447 (1972).
[53] T. Satoh, S.-J. Cho, R. Iida, T. Shimura, K. Kuroda, H. Ueda, Y. Ueda, B. A. Ivanov, F. Nori, and M. Fiebig, Phys. Rev. Lett. **105**, 077402 (2010).
[54] S. Blundell, *Magnetism in Condensed Matter* (Oxford University Press, Oxford, 2001), pp. 94–96.
[55] F. L. A. Machado, P. R. T. Ribeiro, J. Holanda, R. L. Rodríguez-Suárez, A. Azevedo, and S. M. Rezende, Phys. Rev. B **95**, 104418 (2017).
[56] S. Iihama, T. Taniguchi, K. Yakushiji, A. Fukushima, Y. Shiota, S. Tsunegi, R. Hiramatsu, S. Yuasa, Y. Suzuki, and H. Kubota, Nat. Electron. **1**, 120 (2018).
[57] S.-h. C. Baek, V. P. Amin, Y.-W. Oh, G. Go, S.-J. Lee, G.-H. Lee, K.-J. Kim, M. D. Stiles, B.-G. Park, and K.-J. Lee, Nat. Mater. **17**, 509 (2018).
[58] P. Vaidya, S. A. Morley, J. V. Tol, Y. Liu, R. Cheng, A. Brataas, D. Lederman, and E. D. Barco, Science **368**, 160 (2020).
[59] S. M. Rezende, A. Azevedo, and R. L. Rodríguez-Suárez, J. Appl. Phys. **126**, 151101 (2019).
[60] M. Hagiwara, K. Katsumata, H. Yamaguchi, M. Tokunaga, I. Yamada, M. Gross, and P. Goy, Int. J. Infr. Millim. Waves **20**, 617 (1999).
[61] J. P. Kotthaus and V. Jaccarino, Phys. Rev. Lett. **28**, 1649 (1972).
[62] Y.-H. Zhang, T.-C. Chuang, D. Qu, and S.-Y. Huang, Phys. Rev. B **105**, 094442 (2022).
[63] S. Foner, Phys. Rev. **130**, 183 (1963).
[64] R. Y. Umetsu, A. Sakuma, and K. Fukamichi, Appl. Phys. Lett. **89**, 052504 (2006).
[65] Z. Lu, Roman V. Chepulskii, and W. H. Butler, Phys. Rev. B **81**, 094437 (2010).
[66] C. S. Severin, C. W. Chen, and C. Stassis, J. Appl. Phys. **50**, 4259 (1979).
[67] E. Krén, C. Kádár, L. Pál, J. Sólyom, P. Szabó, and T. Tarnóczi, Phys. Rev. **171**, 574 (1968).
[68] R. Y. Umetsu, K. Fukamichi, and A. Sakuma, Mater. Trans. **47**, 2 (2006).
[69] J. Fischer, O. Gomonay, R. Schlitz, K. Ganzhorn, N. Vlietstra, M. Althammer, H. Huebl, M. Opel, R. Gross, S. T. B. Goennenwein, and S. Geprägs, Phys. Rev. B **97**, 014417 (2018).
[70] S. Yu. Bodnar, L. Šmejkal, I. Turek, T. Jungwirth, O. Gomonay, J. Sinova, A. A. Sapozhnik, H.-J. Elmers, M. Kläui, and M. Jourdan, Nat. Commun. **9**, 348 (2018).
[71] A. B. Shick, S. Khmelevskyi, O. N. Mryasov, J. Wunderlich, and T. Jungwirth, Phys. Rev. B **81**, 212409 (2010).
[72] B. G. Park, J. Wunderlich, X. Martí, V. Holý, Y. Kurosaki, M. Yamada, H. Yamamoto, A. Nishide, J. Hayakawa, H. Takahashi, A. B. Shick, and T. Jungwirth, Nat. Mater. **10**, 347 (2011).
[73] O. R. Sulymenko, O. V. Prokopenko, V. S. Tyberkevych, and A. N. Slavin, IEEE Magn. Lett. **9**, 3104605 (2018).
[74] L. López-Mir, C. Frontera, H. Aramberri, K. Bouzehouane, J. Cisneros-Fernández, B. Bozzo, L. Balcells, and B. Martínez, Sci. Rep. **8**, 861 (2018).
[75] P. Merodio, A. Kalitsov, M. Chshiev, and J. Velev, Phys. Rev. Appl. **5**, 064006 (2016).
[76] P. A. Popov, A. R. Safin, A. Kirilyuk, S. A. Nikitov, I. Lisenkov, V. Tyberkevich, and A. Slavin, Phys. Rev. Appl. **13**, 044080 (2020).
[77] P.-H. Chang, W. Fang, T. Ozaki, and K. D. Belashchenko, Phys. Rev. Mater. **5**, 054406 (2021).
[78] E. J. Routh, *A Treatise on the Stability of a Given State of Motion: Particularly Steady Motion* (Macmillan and Co., London, 1877).
[79] A. Hurwitz, Math. Ann. **46**, 273 (1895).
[80] P. Baláž and J. Barnaś, Phys. Rev. B **88**, 014406 (2013).